arXiv:hep-ph/0407298v1 26 Jul 2004

Jet Photoproduction in Peripheral Heavy-Ion Collisions

R. Vogt
Nuclear Science Division, Lawrence Berkeley National Laboratory, Berkeley, CA, 94720
and
Physics Department, University of California, Davis, CA, 95616

Abstract

In peripheral relativistic heavy ion collisions at the Large Hadron Collider, jet+jet and photon+jet final states can be produced when a photon from the virtual photon field surrounding the nucleus interacts with a parton in the opposite nucleus (direct production). The virtual photon may also fluctuate into states with multiple gluons and $q\overline{q}$ pairs (resolved production), opening more channels for jet photoproduction. We compare the rates for direct and resolved jet+jet and photon+jet production to explore the sensitivity to the nuclear and photon parton distribution functions. We calculate the transverse momentum distributions of both partonic jets and leading hadrons produced by jet fragmentation.

I. INTRODUCTION

We discuss measurements of the nuclear parton distributions via dijet (jet+jet) and γ+jet photoproduction in ultraperipheral heavy ion collisions at the Large Hadron Collider (LHC). In these collisions, the accelerated ion is surrounded by a cloud of almost real photons of virtuality $|q^2| < (\hbar c/R_A)^2$ where R_A is the nuclear radius. The virtuality, less than $(60\,\mathrm{MeV})^2$ for nuclei with $A > 16$, can be neglected. Since photon interactions are long range, they can interact with partons in the opposite nucleus even when the nuclei themselves do not interpenetrate. Because the photon energies are less than those of the nucleons, these photonuclear interactions have a smaller average center of mass energy than hadronic parton-parton collisions. However, even though the energy is smaller, the coherent photon beams have a flux proportional to the square of the nuclear charge, Z, enhancing the rates relative to those of photoproduction in pp collisions at the same energy. Thus photoproduction rates in heavy ion collisions can be high.

Photoproduction occurs two ways in heavy ion collisions: “direct” and “resolved” production. “Direct” photoproduction occurs when a photon emitted from one nucleus interacts with a parton from the other nucleus. The photon can also fluctuate into states with multiple $q\overline{q}$ pairs and gluons, *i.e.* $|n(q\overline{q})m(g)\rangle$. One of these photon components can interact with a quark or gluon from the target nucleus (“resolved” production) [1]. The photon components are described by parton densities similar to those used for protons except that no useful momentum sum rule applies to the photon [2]. The quark and gluon constituents of the photon open up more channels for jet photoproduction and could, in principle, lead to larger rates for resolved production in certain regions of phase space.

In central collisions at RHIC, leading particles in jets are easier to detect above the high charged particle multiplicity background than the jets themselves since these high transverse momentum, p_T, particles can be tracked through the detector [3,4]. In peripheral collisions, especially at LHC energies, jets should be easier to isolate and may be observed directly using standard high energy jet detection techniques. We thus discuss the p_T distributions of both jets and leading particles. We work at leading order, LO, to avoid any ambiguities such as jet reconstruction and cone size. The ratio of the next-to-leading order, NLO, to LO jet cross sections appears to be relatively constant at high p_T [5]. We discuss the fragmentation of jets and present the transverse momentum distributions of charged pions, charged kaons and protons/antiprotons.

II. DIJET PRODUCTION

A. Direct dijet production

The first hadronic reaction we study is $\gamma(k)+N(P_2) \rightarrow \mathrm{jet}(p_1) + \mathrm{jet}(p_2) + X$ where k and P_2 are the photon and nucleon four-momenta. The diagrams for direct and resolved dijet hadroproduction are given in Fig. 1. The two parton-level contributions to the jet yield in direct photoproduction are $\gamma(k)+g(x_2P_2) \rightarrow q(p_1)+\overline{q}(p_2)$ and $\gamma(k)+q(x_2P_2) \rightarrow g(p_1)+q(p_2)$ where also $q \rightarrow \overline{q}$. The produced partons are massless, requiring a minimum p_T to keep the cross section finite. At LO, the jet yield is equivalent to the high p_T parton yield. The jet p_T distribution is modified for photoproduction from *e.g.* Refs. [6–8],

$$S^2_{NN} \frac{d^2\sigma^{\rm dir}_{\gamma A \rightarrow {\rm jet}\,+\,{\rm jet}+X}}{dTdUd^2b} = 2\int dz \int_{k_{\rm min}}^{\infty} dk \frac{d^3N_\gamma}{dkd^2b} \int_{x_{2_{\rm min}}}^{1} \frac{dx_2}{x_2} \Bigg[\sum_{i,j,l=q,\overline{q},g} F_i^A(x_2,\mu^2,\vec{b},z) s^2 \frac{d^2\sigma_{\gamma i \rightarrow jl}}{dtdu} \Bigg] \ , \quad (1)$$

where x_2 is the fraction of the initial hadron momentum carried by the interacting parton and μ is the momentum scale of the interaction. Recall that the extra factor of two on the right-hand side of Eq. (1) arises because both nuclei can serve as photon sources in AA collisions. The partonic cross sections are

$$s^2 \frac{d^2\sigma_{\gamma g \rightarrow q\overline{q}}}{dtdu} = \pi\alpha_s(\mu^2)\alpha e_Q^2 \left[\frac{t^2+u^2}{tu}\right] \delta(s+t+u) \ , \quad (2)$$

$$s^2 \frac{d^2\sigma_{\gamma q \rightarrow gq}}{dtdu} = -\frac{8}{3}\pi\alpha_s(\mu^2)\alpha e_Q^2 \left[\frac{s^2+t^2}{st}\right] \delta(s+t+u) \ . \quad (3)$$

The first is the photon-gluon fusion cross section, the only contribution to massive $Q\overline{Q}$ photoproduction [9], while the second is the QCD Compton process. At LO, the partonic cross section is proportional to $\alpha\alpha_s(\mu^2)e_Q^2$, where $\alpha_s(\mu^2)$ is the strong coupling constant to one loop, $\alpha = e^2/\hbar c$ is the electromagnetic coupling constant, and e_Q is the light quark charge, $e_u = e_c = 2/3$ and $e_d = e_s = -1/3$. The partonic invariants, s, t, and u, are defined as $s = (k + x_2P_2)^2$, $t = (k - p_1)^2 = (x_2P_2 - p_2)^2$, and $u = (x_2P_2 - p_1)^2 = (k - p_2)^2$. In this case, $s = 4k\gamma_L x_2 m_p$ where γ_L is the Lorentz boost of a single beam and m_p is the proton mass. Since k can be a continuum of energies up to $E_{\rm beam} = \gamma_L m_p$, we define $x_1 = k/P_1$, analogous to the parton momentum fraction in the nucleon where P_1 is the nucleon four momentum. For a detected parton in a nucleon-nucleon collision, the hadronic invariants are then $S_{NN} = (P_1 + P_2)^2$, $T = (P_2 - p_1)^2$, and $U = (P_1 - p_1)^2$.

The produced parton rapidities are y_1 and y_2. The jet parton rapidity is related to the invariant T by $T = -\sqrt{S_{NN}} p_T e^{-y_1}$. At LO, $x_1 = (p_T/\sqrt{S_{NN}})(e^{y_1} + e^{y_2})$ and $x_2 = (p_T/\sqrt{S_{NN}})(e^{-y_1} + e^{-y_2})$. We calculate x_1 and x_2 as in an NN collision and then determine the flux in the lab frame for $k = x_1 \gamma_L m_p$, equivalent to the center of mass frame in a collider. The photon flux is exponentially suppressed for $k > \gamma_L \hbar c/R_A$, corresponding to a momentum fraction $x_1 > \hbar c/m_p R_A$. The maximum γN center of mass energy, $\sqrt{S_{\gamma N}}$, is much lower than the hadronic $\sqrt{S_{NN}}$. The equivalent hadronic invariants can be defined for photon four momentum k as $S_{\gamma N} = (k + P_2)^2$, $T_{\gamma N} = (P_2 - p_1)^2$, and $U_{\gamma N} = (k - p_1)^2$ [10]. The partonic and equivalent hadronic invariants for fixed k are related by $s = x_2 S_{\gamma N}$, $t = U_{\gamma N}$, and $u = x_2 T_{\gamma N}$.

The photon flux is given by the Weizsäcker-Williams method. The flux from a charge Z nucleus at a distance r is

$$\frac{d^3 N_\gamma}{dk d^2 r} = \frac{Z^2 \alpha w^2}{\pi^2 k r^2} \left[K_1^2(w) + \frac{1}{\gamma_L^2} K_0^2(w) \right] \tag{4}$$

where $w = kr/\gamma_L$ and $K_0(w)$ and $K_1(w)$ are modified Bessel functions. The photon flux decreases exponentially above a cutoff energy determined by the nuclear size. In the lab frame, the cutoff is $k_{\rm max} \approx \gamma_L \hbar c/R_A$. In the rest frame of the target nucleus, the cutoff is boosted to $E_{\rm max} = (2\gamma_L^2 - 1)\hbar c/R_A$. Table I shows, for AA collisions at the LHC, the nucleon-nucleon center of mass energies, $\sqrt{S_{NN}}$, the beam energies, $E_{\rm beam}$, Lorentz factors, γ_L, maximum photon energies in the lab and rest frames, $k_{\rm max}$ and $E_{\rm max}$ respectively, as well as the corresponding maximum $\gamma p \rightarrow q\overline{q}$ center of mass energy, $\sqrt{S_{\gamma N}} = \sqrt{2E_{\rm max} m_p}$, for single photon interactions with protons. We have also included the AA luminosities in Table I to aid the calculation of rates.

The total photon flux striking the target nucleus is the integral of Eq. (4) over the transverse area of the target for all impact parameters subject to the constraint that the two nuclei do not interact hadronically [11]. This must be calculated numerically. However, an analytic approximation for AA collisions is given by the photon flux integrated over distances $r > 2R_A$,

$$\frac{dN_\gamma}{dk} = \frac{2Z^2\alpha}{\pi k} \left[w_R K_0(w_R) K_1(w_R) - \frac{w_R^2}{2} (K_1^2(w_R) - K_0^2(w_R)) \right] \tag{5}$$

where $w_R = 2kR_A/\gamma_L$. The difference between the numerical calculation and the analytic results is typically less than 15% except for photon energies near the cutoff. We use the more accurate numerical calculations.

The nuclear parton densities $F_i^A(x, \mu^2, \vec{b}, z)$ can be factorized into x and μ^2 independent nuclear density distributions, position and nuclear-number independent nucleon parton densities, and a shadowing function $S_A^i(x, \mu^2, \vec{b}, z)$ that describes the modification of the nuclear parton distributions in position and momentum space. Then [6,12–15]

$$F_i^A(x, \mu^2, \vec{b}, z) = \rho_A(\vec{b}, z) S_A^i(x, \mu^2, \vec{b}, z) f_i^N(x, \mu^2) \tag{6}$$

where $f_i^N(x,\mu^2)$ is the parton density in the nucleon. We use the MRST LO parton distributions [16] at $\mu^2 = p_T^2$. In the absence of nuclear modifications, $S^i \equiv 1$. The nuclear density distribution, $\rho_A(\vec{b},z)$, is a Woods-Saxon with parameters determined from electron scattering data [17]. Although most models of shadowing predict a dependence on the parton position in the nucleus, we neglect any impact parameter dependence here so that $S_A^i(x,\mu^2,\vec{b},z) \rightarrow S_A^i(x,\mu^2)$.

The nuclear modification, collectively referred to as shadowing here, encompasses three x regions: low x shadowing where $S_A^i < 1$, $x < 0.01$; antishadowing where $S_A^i > 1$, $0.01 \leq x \leq 0.1$ and the EMC region where again $S_A^i < 1$ but $x \geq 0.2$. We use two parameterizations of nuclear shadowing which cover extremes of low x gluon shadowing. The Eskola *et al.* parameterization, EKS98, is based on the GRV LO [18] parton densities. At the minimum scale, μ_0, valence quark shadowing is identical for u and d quarks. Likewise, the shadowing of $\overline{u}$ and $\overline{d}$ quarks are identical at μ_0. Although the light quark shadowing ratios are not constrained to be equal at higher scales, the differences between them are small. Shadowing of the heavier flavor sea, $\overline{s}$ and higher, is calculated separately at μ_0. The shadowing ratios for each parton type are evolved to LO for $1.5 < \mu < 100$ GeV and are valid for $x \geq 10^{-6}$ [19,20]. Interpolation in nuclear mass number allows results to be obtained for any input A. The parameterization by Frankfurt, Guzey and Strikman, FGS, combines Gribov theory with hard diffraction [21]. It is based on the CTEQ5M [22] parton densities and evolves each parton species separately to NLO for $2 < \mu < 100$ GeV. Although the given x range is $10^{-5} < x < 0.95$, the sea quark and gluon ratios are unity for $x > 0.2$ and μ_0. The EKS98 valence quark shadowing ratios are used as input at μ_0 since Gribov theory does not predict valence shadowing. The parameterization is available for four different values of A: 16, 40, 110 and 206.

Figure 2 compares the two parameterizations for $A \approx 200$ and $\mu = 10$, 100 and 400 GeV. Some care must be taken when applying these parameterizations to high p_T since the upper limit of their fit range is 100 GeV. The valence ratios, identical for EKS98 and FGS at μ_0, are somewhat different at high scales because the evolution is different, LO for EKS98 and NLO for FGS. The sea quark ratios are rather dissimilar. The EKS98 ratios have no antishadowing but, instead, show a peak at $S_A^{\overline{u}} \approx 1$ when $x \approx 1$, decreasing smoothly at larger x, the EMC region. The FGS parameterization has an antishadowing peak at $x \approx 0.07$ after which $S_A^{\overline{u}} \approx 1$ for $x > 0.2$, as at μ_0. Thus quark shadowing in the EMC x region will be stronger for EKS98. At the lowest x and μ shown, the FGS gluon ratio shows stronger shadowing and larger antishadowing than EKS98. By $\mu \geq 100$ GeV, the results are rather similar. It is notable that at μ_0 the FGS gluon ratio is ≈ 1 for $x > 0.2$ and decreases below 1 at higher scales, unlike the sea quark ratios, exhibiting an EMC-like effect. At high p_T, therefore, the EKS98 and FGS gluon ratios should not be significantly different. As we have already pointed out, although the upper limit on the range of both shadowing parameterizations is 100 GeV, the parameterizations do not strongly deviate from the trends at lower scales. Thus the results can be taken as indicative of the expected behavior.

There are a few photon parton distributions available [23–29]. The data [30,31] cannot definitively rule out any of these parton densities. As expected, $F_q^\gamma(x,\mu^2) = F_{\overline{q}}^\gamma(x,\mu^2)$ flavor by flavor because there are no "valence" quarks in the photon. The gluon distribution in the photon is less well known. We use the GRV-G LO set [23,24]. At $p_T > 10$ GeV, the difference in results due to the photon parton densities is minimal.

The direct jet photoproduction p_T distributions are given in Fig. 3 for AA interactions at the LHC. For Pb+Pb collisions at $\sqrt{S_{NN}} = 5.5$ TeV, we show the p_T distributions of the produced quarks, antiquarks and gluons separately, as well as their sum. For Ar+Ar collisions at $\sqrt{S_{NN}} = 6.3$ TeV and O+O collisions at $\sqrt{S_{NN}} = 7$ TeV, we show only the total p_T distributions. All the results are shown in the rapidity interval $|y_1| \leq 1$.

Quarks and antiquarks are produced in greatest abundance, with only a small difference at high p_T. Photon-gluon fusion alone produces equal numbers of quarks and antiquarks. The quark excess arises from the QCD Compton diagram which also produces the small final-state gluon contribution. The $\gamma(q + \overline{q})$ contribution grows with p_T since the valence quark distributions eventually dominate production, as shown in Fig. 3(b) where the γg contribution is compared to the total. At low p_T, the γg contribution is $\approx 90\%$ of the total, dropping to $10 - 30\%$ at $p_T \approx 400$ GeV. At the large values of x needed for high p_T jet production, $f_p^{u_V} > f_p^g$. Thus the QCD Compton process eventually dominates dijet production, albeit in a region of very low statistics. The γg contribution is larger for the lighter nuclei since the higher energies reduce the average x values.

The direct dijet photoproduction cross section is significantly lower than the hadroproduction cross section. Some of this reduction is due to the different couplings. The photoproduction rate is reduced by a factor of $\alpha e_Q^2/\alpha_s \approx 100$. There are also fewer diagrams available for jet photoproduction relative to all $2 \rightarrow 2$ scatterings in hadroproduction. In addition, the $gg \rightarrow gg$ hadroproduction process, with its high parton luminosity, has no direct photoproduction equivalent.

Since the typical scales of jet production are large, the effects of shadowing, reflected in $R(p_T) = (d\sigma[S_A^i]/dp_T)/(d\sigma[S_A^i = 1]/dp_T)$, are rather small, see Fig. 3(c) and (d), because the average x is high. The differences between the two shadowing parameterizations are on the few percent level. At low p_T, the produced quarks and antiquarks are mainly from gluons. The produced gluons only come from quarks. The peak for the produced quarks and antiquarks in $R(p_T)$ between $50 \leq p_T \leq 100$ GeV is due to gluon antishadowing. The total $R(p_T)$ for all produced partons in Pb+Pb collisions is dominated by the γg contribution. The maximum value of S_A^i in the antishadowing region is ≈ 1.07 for EKS98 and ≈ 1.1 for FGS, reflecting the high μ^2 behavior of the shadowing parameterizations.

The EKS98 ratios for the produced quarks and antiquarks in Fig. 3(c) follow $R(p_T)$ for the total rather closely over all p_T. The quark and antiquark ratios are slightly above the total at low p_T due to the small γq contribution. They continue to follow the total at high p_T since all the EKS98 ratios exhibit similar behavior at large x. The produced gluon ratio follows the quark ratios for $p_T > 200$ GeV. The large p_T contribution arises from the valence quarks. Some antishadowing is observed at low p_T due to the valence quark contribution. The total ratios for the lighter ions are closer to unity for all p_T due to their smaller A.

The results are similar for FGS, shown in Fig. 3(d), but there are some subtle differences. The ratio $R(p_T)$ for produced gluons, arising from the γq contribution, exhibits a larger antishadowing effect on $R(p_T)$ because $S_A^{\overline{q}}$ is higher for this parameterization, see Fig. 2. The FGS antiquark shadowing ratio goes to unity for $x > 0.2$, flattening $R(p_T)$ for antiquarks (dotted curve) due to the contribution from $\gamma\overline{q} \rightarrow g\overline{q}$. The FGS valence quark ratio is taken from EKS98, resulting in the similarity of $R(p_T)$ in Figs. 3(c) and (d) at high p_T.

Recall that some care must be taken when applying these parameterizations to high p_T since the upper limit of their fit range is 100 GeV. While no extraordinary effects are seen in their behavior beyond this scale, the results should be taken as indicative only. Finally, we remark that we have only considered the range $|y_1| \leq 1$. Including contributions from all rapidities would increase the effect of shadowing since smaller x values can be reached when $|y_1|$ is large.

In Fig. 4, we present the rapidity distributions with two different values of the minimum p_T, $p_T > 10$ GeV on the left-hand side and 100 GeV on the right-hand side. The results, given by the solid curves, are shown without nuclear shadowing effects. Note that, in this case, the photon comes from the left. There is a symmetric case where the photon comes from the right, the factor of two on the p_T distribution in Eq. (1). In this case, the y_1 distribution is reflected around $y_1 = 0$. With the 10 GeV cut, the distributions are rather broad at negative y_1 where the photon has small momentum and, hence, large flux. At large $y_1 > 0$, corresponding to small x for the nucleon momentum fractions and high photon momentum, the distributions fall rapidly since at high photon momenta, the photon flux is cut off as $k \rightarrow k_{\rm max}$. The distributions with the 100 GeV cutoff are narrower because the edge of phase space is reached at lower values of y_1. The rapidity distributions are broader in general for the lighter systems due to the higher $\sqrt{S_{NN}}$.

Figure 5 gives the ratio $R(y_1) = (d\sigma[S_A^i]/dy_1)/(d\sigma[S_A^i = 1]/dy_1)$ for the two p_T cuts. The ratios reflect the direction of the photon, showing an antishadowing peak at $y_1 \sim -3$, an EMC region at $y_1 < -4$ and a shadowing region for $y_1 > -0.5$ for $p_T > 10$ GeV, the left-hand side of Fig. 5. The shadowing effect is not large, $(20 - 25)\%$ at $y_1 \sim 4$ for Pb+Pb collisions and decreasing with A. The antishadowing peak is higher for FGS while its shadowing effect is larger at positive y_1, as also noted in the p_T-dependent ratios in Fig. 3. A comparison of the average effect around $|y_1| \leq 1$ with the p_T ratios shown in Fig. 3, are in good agreement. Even though x_2 is smaller for the lighter systems, the shadowing effect is also reduced. Since shadowing also decreases with μ^2, the effect is even smaller for $p_T > 100$ GeV, only $\sim 5\%$ at $y_1 \geq 0$, as shown on the right-hand side of Fig. 5. Here the rise at $y_1 < -3.5$ is the Fermi motion as $x_2 \rightarrow 1$. At $y_1 > -1.2$, the antishadowing region is reached.

The total dijet photoproduction cross sections without shadowing and the corresponding rates in a one month, 10^6 s, LHC run are shown in Table II. The rates are based on the luminosities of Table I. All results are given in the rapidity interval $|y_1| \leq 1$. Extended rapidity coverage, corresponding to *e.g.* $|y_1| \leq 2.4$ for the CMS barrel and endcap systems, could increase the rates by a factor of ≈ 2. (The increase in rate with rapidity acceptance is not linear in $|y_1|$ because the rapidity distributions are asymmetric around $y_1 = 0$ and increasing p_T narrows the rapidity distribution. The effect of changing the y_1 cut is closer to linear at low p_T and larger at high p_T because the peak is at $y_1 < -1$ for large p_T, as seen in the y_1 distributions on the right-hand side of Fig. 4.) Note that by $p_T \approx 100$ GeV, only a few events are expected per month. However, while high p_T jets are rare, they should be easily observable in a clean environment like photoproduction.

There is a difference of ≈ 500 in the Pb+Pb and O+O cross sections at $p_T \approx 11$ GeV, decreasing to less than a factor of four at ≈ 400 GeV. The difference decreases with p_T due to the larger phase space available at high p_T for the higher $\sqrt{S_{NN}}$ systems. Note that the rates are nearly the same for all systems because even though A is larger for Pb+Pb, higher luminosities and higher $\sqrt{S_{NN}}$ compensates for the lower A in lighter systems.

We point out that the jet hadroproduction rates are much higher because they are multiplied by $\approx A^2$ for hard processes which increase with the number of binary collisions in AA collisions. (The relation is not exact due to shadowing.) The integration over all impact parameters leads to $\approx A^2$ scaling while there is only a factor of A in the dijet photoproduction rate since the photon flux is already integrated over impact parameter for $b > 2R_A$. This, combined with the lower effective energy and fewer channels, considerably reduces the photoproduction rates relative to hadroproduction.

B. Direct leading hadron production

We now turn to a description of the final-state particle production in the hadronization of jets. The particle with the highest p_T is called the "leading" particle. The corresponding leading particle p_T distribution is [32]

$$\frac{d\sigma^{\rm dir}_{\gamma A\rightarrow hX}}{dp_T d^2b} = 4p_T \int dz \int_{\theta_{\rm min}}^{\theta_{\rm max}} \frac{d\theta_{\rm cm}}{\sin\theta_{\rm cm}} \int dk \frac{d^3N_\gamma}{dkd^2b} \int \frac{dx_2}{x_2} \times \Bigg[\sum_{i,l=q,\overline{q},g} F_i^A(x_2,\mu^2,\vec{b},z) \frac{d\sigma_{\gamma i\rightarrow lX'}}{dt} \frac{D_{h/l}(z_c,\mu^2)}{z_c} \Bigg] \tag{7}$$

where the X on the left-hand side includes all final-state hadrons in addition to h but X' on the right-hand side denotes the unobserved final-state parton. The subprocess cross sections, $d\sigma/dt$, are related to $s^2 d\sigma/dtdu$ in Eq. (1) through the momentum-conserving delta function $\delta(s+t+u)$ and division by s^2. The integrals over rapidity have been replaced by an integral over center-of-mass scattering angle, $\theta_{\rm min} \leq \theta_{\rm cm} \leq \theta_{\rm max}$, corresponding to a given rapidity cut. Here $\theta_{\rm min} = 0$ and $\theta_{\rm max} = \pi$ covers the full rapidity range while $\theta_{\rm min} = \pi/4$ and $\theta_{\rm max} = 3\pi/4$ roughly corresponds to $|y_1| \leq 1$. The fraction of the final hadron momentum relative to that of the produced parton, z_c, appears in the fragmentation function, $D_{h/l}(z_c,\mu^2)$, the probability to produce hadron h from parton l. The fragmentation functions are assumed to be universal, independent of the initial state.

The produced partons are fragmented into charged pions, charged kaons and protons/antiprotons using LO fragmentation functions fit to e^+e^- data [33]. The final-state hadrons are assumed to be produced pairwise so that $\pi \equiv (\pi^+ + \pi^-)/2$, $K \equiv (K^+ + K^-)/2$, and $p \equiv (p + \overline{p})/2$. The equality of p and $\overline{p}$ production obviously does not describe low energy hadroproduction well. As energy increases, this approximation may become more reasonable. The produced hadrons follow the parent parton direction. We have used the LO KKP fragmentation functions [33]. The KKP scale evolution is modeled using e^+e^- data at several different energies and compared to $p\overline{p}$, γp and $\gamma\gamma$ data. After some slight scale modifications [34] all the h^- data could be fit. However, there are significant uncertainties in fragmentation when the leading hadron takes most of the parton momentum [35], as is the case here.

We assume the same scale in the parton densities and the fragmentation functions, $\mu^2 = p_T^2$. A larger scale, p_T^2/z_c^2, has sometimes been used in the parton densities. At high p_T, where z_c is large, the difference in the results for the two scales is small. We have not included any intrinsic transverse momentum broadening in our calculations [36,37]. This "Cronin" effect can be important when p_T is small but becomes negligible for transverse momenta larger than a few GeV.

The largest contribution to the total final-state charged particle production is charged pions, followed by kaons. The proton contribution is smallest even though at RHIC the p/π ratio approaches unity in central and 0.4 in peripheral Au+Au collisions [38] for $p_T \sim 2$ GeV. This discrepancy is due to the poor knowledge of the fragmentation functions at large z_c, particularly for baryons. Hopefully by the time the LHC begins operation, updated fragmentation functions incorporating pp data from RHIC will be available, allowing better estimates of leading particle production at higher z_c.

The corresponding hadron distributions from direct jet photoproduction are shown in Fig. 6(a) for AA collisions. Note that the leading hadron cross sections are lower than the partonic jet cross sections, compare Figs. 3(a) and 6(a). Several factors can account for this. The maximum $\sqrt{S_{\gamma N}}$ is a factor of five or more less than $\sqrt{S_{NN}}$ for AA collisions. The reduced number of processes available for direct dijet photoproduction is a significant contribution to the decrease. Note also that the p_T distribution is steeper for leading hadrons than for the jets, as may be expected since the effective p_T of the hadron is higher than than of the produced parton.

The average z_c for direct photoproduction of high p_T particles is ≈ 0.4 for particles with $p_T \approx 10$ GeV, increasing to $\langle z_c \rangle > 0.45 - 0.55$ for $p_T > 100$ GeV. The lower z_c values correspond to lighter ion collisions. In this z_c region, the fragmentation functions are not very well known. As pointed out in Ref. [35], a small change in the fragmentation function fits can produce significant changes at large z_c. This region is not well constrained by the e^+e^- data used in the fits.

The effect of fragmentation on the production channels is shown in Fig. 6(b) where we present the fraction of leading hadron production from the γg channel for all charged hadrons. The ratios are rather similar to those of the partonic jets although the γg fraction is somewhat smaller due to the larger average x of hadron production with respect to jets, as we discuss later.

The shadowing ratios for charged pions produced in Pb+Pb collisions by quarks, antiquarks, gluons and the total from all partons, are shown for the EKS98 and FGS parameterizations in Fig. 6(c) and (d). The ratios for pion production in Ar+Ar and O+O collisions are also shown. The high p_T FGS antiquark ratios flatten out relative to the EKS98 ratio because the $\gamma \overline{q}$ channel dominates gluon production at high p_T. The flattening begins at lower p_T here because the x for hadron production is higher than that for the jets. The ratio of pions arising from produced gluons follows the valence ratio, as expected. The ratios decrease with increasing p_T due to the EMC effect for $x > 0.2$ when $p_T > 100$ GeV.

We now discuss the relative values of the nucleon momentum fraction, x for parton and hadron production. On the left-hand side of Fig. 7, we compare the average x values for produced gluon jets (upper plot) and for pions produced by these gluons (lower plot). We have chosen to compute the results for produced gluons alone to better compare with resolved jet photoproduction, discussed next. Since we are interested in produced gluons, we only consider the QCD Compton contribution, $\gamma q \to gq$. This channel is biased toward larger momentum fractions than $\gamma g \to q\overline{q}$ since the gluon distribution is largest at small x while the valence quark distribution in the proton is peaked at $x \sim 0.2$. The average x for a gluon jet is $\sim 0.005 - 0.008$ at $p_T \approx 10$ GeV, increasing to $\sim 0.03 - 0.05$ at 50 GeV. The smallest x is from the highest energy O+O collisions. The average x increases with p_T, to $\sim 0.25 - 0.4$ at $p_T \sim 400$ GeV. When final state pions are considered, in the lower left-hand plot, at low p_T, the average x is larger than for gluon jets. At $p_T \approx 10$ GeV, $\langle x \rangle \approx 0.02-0.03$ while at 50 GeV, $\langle x \rangle \approx 0.09 - 0.12$. At high p_T, however, the average x becomes similar for jet and hadron production as $\langle z_c \rangle$ increases to $\approx 0.6 - 0.7$ at $p_T \sim 400$ GeV.

C. Resolved dijet production

We now turn to resolved production. The hadronic reaction, $\gamma N \rightarrow \mathrm{jet} + \mathrm{jet} + X$, is unchanged, but in this case, prior to the interaction with the nucleon, the photon splits into a color singlet state of $q\overline{q}$ pairs and gluons. On the parton level, the resolved LO reactions are *e.g.* $g(xk)+g(x_2P_2) \rightarrow g(p_1)+g(p_2)$ where x is the fraction of the photon momentum carried by the parton. The LO processes for resolved photoproduction, illustrated in Fig. 1(c)-(h), are the same as those for LO $2 \rightarrow 2$ hadroproduction except that one parton source is a photon rather than a nucleon. The resolved jet photoproduction cross section for partons of flavor f in the subprocess $ij \rightarrow kl$ in AB collisions is, modified from Refs. [6–8],

$$S^2_{NN} \frac{d\sigma^{\mathrm{res}}_{\gamma A \rightarrow \mathrm{jet}+\mathrm{jet}}}{dT dU d^2b} = 2 \int dz \int_{k_{\mathrm{min}}}^{\infty} \frac{dk}{k} \frac{d^3N_\gamma}{dk d^2b} \int_{k_{\mathrm{min}}/k}^{1} \frac{dx}{x} \int_{x_{2_{\mathrm{min}}}}^{1} \frac{dx_2}{x_2}$$

$$\times \sum_{\substack{ij= \\ \langle kl \rangle}} \left\{ F_i^\gamma(x,\mu^2) F_j^A(x_2,\mu^2,\vec{b},z) + F_j^\gamma(x,\mu^2) F_i^A(x_2,\mu^2,\vec{b},z) \right\}$$

$$\times \frac{1}{1+\delta_{kl}} \left[\delta_{fk} \hat{s}^2 \frac{d\sigma^{ij\rightarrow kl}}{d\hat{t} d\hat{u}}(\hat{t},\hat{u}) + \delta_{fl} \hat{s}^2 \frac{d\sigma^{ij\rightarrow kl}}{d\hat{t} d\hat{u}}(\hat{u},\hat{t}) \right] \quad (8)$$

where $\hat{s} = (xk + x_2P_2)^2$, $\hat{t} = (xk - p_1)^2$, and $\hat{u} = (x_2P_2 - p_1)^2$. The $2 \rightarrow 2$ minijet subprocess cross sections, $d\sigma/d\hat{t}$, given in the review article by Owens [39], are related to $d\sigma/d\hat{t}d\hat{u}$ through the momentum-conserving delta function $\delta(\hat{s}+\hat{t}+\hat{u})$. The sum over initial states includes all combinations of two parton species with three flavors while the final state includes all pairs without a mutual exchange and four flavors (including charm). The factor $1/(1 + \delta_{kl})$ accounts for identical particles in the final state.

The resolved jet results, shown in Fig. 8, are independent of the photon parton densities for $p_T > 10$ GeV. Along with the total quark, antiquark and gluon cross sections in Pb+Pb collisions, we also show the individual partonic contributions to the jet p_T distributions. The produced gluon contribution dominates for $p_T < 25$ GeV but, by 50 GeV, quark and antiquark production becomes larger due to the increase of the $qg \rightarrow qg$ channel relative to the $gg \rightarrow gg$ channel. We also show the total p_T distributions for Ar+Ar and O+O collisions. For lighter nuclei, the crossover between gluon and quark/antiquark dominance occurs at higher p_T due to the higher collision energy.

Note that the resolved dijet photoproduction contribution is larger than the direct by a factor of two to three for $p_T < 50$ GeV, despite the lower effective center of mass energy of resolved production. Resolved production opens up many more channels through the parton components of the photon. Indeed, now all the $2 \rightarrow 2$ channels for LO jet hadroproduction are available. In addition, the quark and antiquark distributions in the photon are the same. These distributions are large at high momentum fractions, higher than the quark and antiquark distributions in the proton. Thus the quark and antiquark channels are enhanced relative to hadroproduction. The largest difference between the quark and antiquark production rates is due to the difference between the valence and sea quark distributions in the nucleus. Where the valence and sea quark contributions are similar, as for $|y_1| \leq 1$, the difference is rather small. If all rapidities were included, the relative quark and antiquark rates could differ more.

The direct and resolved rapidity distributions are compared in Fig. 4 for the two p_T cuts, 10 and 100 GeV. While the $|y_1| \leq 1$ resolved contribution is a factor of two to three larger than the direct at $p_T < 50$ GeV, a comparison of the y_1 distributions over all rapidities shows that the resolved contribution can be considerably larger, a factor of $\sim 5-10$ at $y_1 < -3.5$ for $p_T > 10$ GeV. At $p_T > 100$ GeV, the resolved contribution is still equivalent to or slightly larger than the direct at $y_1 < -3$ but drops below at larger rapidities. Thus, going to higher p_T can separate direct from resolved production, especially at forward rapidities. Recall that the produced gluons dominate resolved production at $p_T < 25$ GeV while they are only a small contribution to direct production. The largest gluon production channels are typically $gg \to gg$ and $gq \to gq$. As y_1 becomes large and negative, the photon x decreases while x_2 of the nucleon increases, leading to the dominance of the gq channel. The photon gluon distribution is largest as x decreases. The valence quark distribution of the proton is also important at high p_T, causing the resolved to direct ratio to flatten for $y_1 > -2.5$ when $p_T > 100$ GeV.

In Fig. 5, we compare the direct and resolved shadowing ratios, $R(y_1)$. A smaller shadowing effect is observed for the resolved component due to the larger x_2 for resolved production. The difference in the direct and resolved shadowing ratios is reduced for larger p_T.

To measure the nuclear parton densities most directly, it is preferable for direct production to be dominant. However, Fig. 9 shows that a p_T cut is not very effective for dijet production, as previously mentioned, even at forward rapidity. The resolved to direct production ratios are all larger than unity for $p_T > 10$ GeV, even for large, positive y_1. While the ratio is less than 1 for $y_1 > -2.5$ and $p_T > 100$ GeV, it is only ~ 0.5 for Pb+Pb, increasing to 0.8 for O+O.

Thus, although clean separation is possible at $p_T > 100$ GeV, precision parton density measurements are not possible at these values of p_T due to the low rate. Other means of separation must then be found. Resolved processes will not be as clean as direct in the direction of the photon due to the breakup of the partonic state of the photon. The multiplicity in the photon fragmentation region will be higher than in direct production where the nucleus should remain intact. A cut on multiplicity in the photon direction may help separate the two so that, although there should be a rapidity gap for both direct and resolved photoproduction, the gap may be less prominent for resolved production.

The total resolved dijet photoproduction cross sections without shadowing and the corresponding monthly (10^6 s) LHC rates are given in Table III. At low p_T, the cross sections and rates are a factor of $2-3$ higher than for direct dijet production. The largest increase is for the lightest nuclei since the lowest x values are probed. However, with increasing p_T, the phase space is reduced. The average photon momentum is increased and, at large photon momentum, the flux drops faster. The average momentum fractions probed by the nuclear parton densities grows large and only valence quarks contribute. The lower effective energy of resolved relative to direct photoproduction reduces the high p_T phase space for resolved production. Thus, at the highest p_T, the rate is reduced relative to direct by a factor of $4-9$ with the smallest decrease for the lightest system due to the higher effective $\sqrt{S_{NN}}$. Since resolved production has a narrower rapidity distribution than direct production, increasing the rapidity coverage would not increase the rate as much as for direct photoproduction.

We show the individual partonic shadowing ratios for Pb+Pb collisions with the EKS98 parameterization in Fig. 8(b). The quark and antiquark shadowing ratios are very similar although the quark ratio becomes larger for higher p_T (higher x) values of x due to the valence distribution. Now the gluon ratio shows larger antishadowing since gluon production is dominantly through the gg and qg channels rather than γq in direct production, compare Fig. 3. The FGS parameterization gives similar results, Fig. 8(c). However, since the small FGS gluon antishadowing is stronger, $R(p_T)$ is larger for $p_T < 150$ GeV.

D. Resolved leading particle production

We now turn to leading particles from resolved jet photoproduction. The leading particle p_T distributions are

$$\begin{aligned}\frac{d\sigma^{\rm res}_{\gamma A\rightarrow hX}}{dp_T d^2b} &= 4p_T \int dz \int_{\theta_{\rm min}}^{\theta_{\rm max}} \frac{d\theta_{\rm cm}}{\sin\theta_{\rm cm}} \int_{k_{\rm min}}^{\infty} \frac{dk}{k}\frac{d^3N_\gamma}{dkd^2b} \int_{k_{\rm min}/k}^{1} \frac{dx}{x} \int_{x_{2_{\rm min}}}^{1} \frac{dx_2}{x_2} \\ &\times \sum_{\substack{ij= \\ \langle kl\rangle}} \left\{F_i^\gamma(x,\mu^2)F_j^A(x_2,\mu^2,\vec{b},z) + F_j^\gamma(x,\mu^2)F_i^A(x_2,\mu^2,\vec{b},z)\right\} \\ &\times \frac{1}{1+\delta_{kl}}\left[\delta_{fk}\frac{d\sigma^{ij\rightarrow kl}}{d\hat{t}}(\hat{t},\hat{u}) + \delta_{fl}\frac{d\sigma^{ij\rightarrow kl}}{d\hat{t}}(\hat{u},\hat{t})\right]\frac{D_{h/k}(z_c,\mu^2)}{z_c}\ . \qquad (9)\end{aligned}$$

The subprocess cross sections, $d\sigma/d\hat{t}$, are related to $\hat{s}^2 d\sigma/d\hat{t}d\hat{u}$ in Eq. (8) through the momentum-conserving delta function $\delta(\hat{s}+\hat{t}+\hat{u})$ and division by $\hat{s}^2$. The drop in rate between jets and high p_T hadrons is similar to that in direct photoproduction, as can be seen by comparison of Figs. 8 and 10 relative to Figs. 3 and 6. Now that gluon fragmentation makes a larger contribution, the relative pion contribution is larger than in direct photoproduction while the relative proton contribution is significantly reduced. The smaller effective center of mass energy for resolved photoproduction lowers the phase space available for fragmentation. Baryon production is then reduced compared to light mesons.

The reduction in phase space for leading hadrons relative to fast partons can be seen in the comparison of the average x values for resolved photoproduction of jets and leading hadrons, shown on the right-hand side of Fig. 7 for gluons and pions from gluons respectively. At $p_T \approx 10$ GeV, the average x of the gluon jet is $0.03 - 0.04$, increasing to $0.16 - 0.24$ at $p_T \approx 200$ GeV, higher than for direct photoproduction, as expected. The x values for hadron production are larger still, ≈ 0.06 at low p_T while $x \approx 0.23 - 0.33$ at $p_T \approx 200$ GeV.

The shadowing ratios in Fig. 10 also reflect the increasing x. Now the antishadowing peak is shifted to $p_T \approx 30$ GeV since the average x values are in the EMC region, even at low p_T. The values of $R(p_T)$ at high p_T are somewhat lower than for direct production due to the higher x. The average z_c of the fragmentation functions is also somewhat larger for resolved production, $0.7 - 0.8$ at $p_T \approx 400$ GeV.

Since the resolved jet cross section is larger than the direct at low p_T, it is more difficult to make clean measurements of the nuclear gluon distribution unless the two contributions can be separated by other methods. Instead, the large valence quark contribution at high p_T suggests that jet photoproduction can probe the nuclear valence quark distributions at larger μ^2 than previously possible. At $p_T > 100$ GeV, more than half of direct jet production is through the γq channel. Unfortunately, the rates are low here, making high precision measurements unlikely. However, the events should be very clean.

III. γ+JET PRODUCTION

A. Direct γ+jet production

A clean method of determining the quark distribution in the nucleus at lower p_T is the process where a jet is produced opposite a photon in the final state, Compton scattering in direct production. The cross sections are reduced relative to the jet+jet process since the coupling is $\alpha^2 e_Q^4$ in the coupling rather than $\alpha\alpha_s e_Q^2$, as in dijet production. In addition, the quark distributions are lower than the gluon, also reducing the rate. The diagrams for γ+jet production are shown in Fig. 11.

We now discuss the jet and leading particle distributions for direct and resolved γ+jet photoproduction. The hadronic process is $\gamma(k) + N(P_2) \to \gamma(p_1) + \mathrm{jet}(p_2) + X$. The only partonic contribution to the γ+jet yield in direct photoproduction is $\gamma(k) + q(x_2P_2) \to \gamma(p_1) + q(p_2)$ (or $q \to \overline{q}$) where the produced quark is massless. We now have

$$S_{NN}^2 \frac{d^2\sigma^{\rm dir}_{\gamma A \to \gamma + \,{\rm jet} + X}}{dTdUd^2b} = 2\int dz \int_{k_{\rm min}}^{\infty} dk \frac{d^3N_\gamma}{dkd^2b} \int_{x_{2_{\rm min}}}^{1} \frac{dx_2}{x_2} \Big[\sum_{i=q,\overline{q}} F_i^A(x_2, \mu^2, \vec{b}, z) s^2 \frac{d^2\sigma_{\gamma i \to \gamma i}}{dtdu} \Big] \quad (10)$$

where the partonic cross section for the Compton process is

$$s^2 \frac{d^2\sigma_{\gamma q \to \gamma q}}{dtdu} = -\frac{2}{3}\pi\alpha^2 e_Q^4 \left[\frac{s^2+u^2}{su}\right] \delta(s+t+u) \ . \quad (11)$$

The extra factor of two on the right-hand side of Eq. (10) again arises because both nuclei can serve as photon sources in AA collisions. The kinematics are the same as in jet+jet photoproduction, described in the previous section.

The direct γ+jet photoproduction results are given in Fig. 12 for AA interactions at the LHC. We show the transverse momentum, p_T, distributions for all produced quarks and antiquarks in Pb+Pb, Ar+Ar and O+O collisions for $|y_1| \leq 1$.

There is a drop of nearly three orders of magnitude between the dijet cross sections in Fig. 3 and the γ+jet cross sections in Fig. 12. Most of this difference comes from the relative couplings. The rest is due to the reduced number of channels available for direct γ+jet production since more than half of all directly produced are gluon-initiated for $p_T < 100$ GeV, see Fig. 3(b).

We have not distinguished between the quark and antiquark initiated jets. However, the quark-initiated jet rate will always be somewhat higher due to the valence contribution. When $p_T < 100$ GeV, the quark and antiquark jet rates are very similar since x is still relatively low. At higher p_T, the valence contribution increases so that when $p_T = 400$ GeV, the quark rate is 1.5 times the antiquark rate. Since the initial kinematics are the same for γ+jet and jet+jet final states, the average momentum fractions for γ+jet production are similar to those shown for the $\gamma q \to gq$ channel in Fig. 7.

The shadowing ratios shown in Fig. 12(b) are dominated by valence quarks for $p_T > 100$ GeV. The FGS ratio is slightly higher because the EKS98 parameterization includes sea quark shadowing. The effect is similar to the produced gluon ratios, at the same values of x in Fig. 3(c) and (d), since the final-state gluons can only come from quark and antiquark induced processes.

We next present the rapidity distributions for the same two p_T cuts used for dijet photoproduction in Fig. 13. Note that the rapidity distribution for $p_T > 10$ GeV is broader at negative y_1 than the dijet distributions in Fig. 4 because direct dijet production is dominated by $\gamma g \rightarrow q\overline{q}$ at these p_T while the valence distribution entering the $\gamma q \rightarrow \gamma q$ does not drop as rapidly at large x_2 as the gluon distribution. When the turnover at large negative y_1 occurs, it is steeper than for the dijets. However, it drops even more steeply at forward y_1 because the quark distribution is smaller than the gluon at low x_2. When $p_T > 100$ GeV, the γ+jet y_1 distribution is narrower than the dijets since the quark distributions drop faster with increasing x_2 at high p_T.

The shadowing ratios as a function of y_1 are shown in Fig. 14. They exhibit some interesting differences from their dijet counterparts in Fig. 5 because of the different production channels. At $p_T > 10$ GeV, the antishadowing peak is lower at $y_1 \sim -2.5$ and the shadowing is larger at $y_1 > 0$. Although this may seem counterintuitive, comparing the valence and sea quark shadowing ratios in Fig. 2 can explain this effect. Valence antishadowing, the same for EKS98 and FGS, is not as strong as that of the gluon. The sea quarks have either no antishadowing (EKS98) or a smaller effect than the valence ratios (FGS). Thus antishadowing is reduced for direct γ+jet production. At large y_1, the x_2 values, while smaller than those shown in Fig. 5(a) for $|y_1| \leq 1$, are still moderate. Since the evolution of the gluon distribution is faster with μ^2, sea quark shadowing is actually stronger than gluon shadowing at $p_T > 10$ GeV and low x_2. When $p_T > 100$ GeV, the Fermi momentum peak is not as prominent because the sharp increase in the valence and sea shadowing ratios appears at higher x_2 than for the gluons, muting the effect, particularly for the lighter systems.

The cross sections and rates in a one month, 10^6 s, run, shown in Table IV, are lower than those for hadroproduction. Direct γ+jet photoproduction proceeds through fewer channels than hadroproduction where the LO channels are $gq \rightarrow \gamma q$ and $q\overline{q} \rightarrow g\gamma$, the same diagrams for resolved γ+jet photoproduction. This, along with the lower effective energy and correspondingly higher x, reduces the photoproduction cross sections relative to hadroproduction. The lower A scaling for photoproduction also restricts the high p_T photoproduction rate.

B. Direct γ+hadron production

We now turn to a description of final-state hadron production opposite a photon. The leading particle p_T distribution is [32]

$$\frac{d\sigma^{\rm dir}_{\gamma A \rightarrow hX}}{dp_T d^2b} = 4p_T \int dz \int_{\theta_{\rm min}}^{\theta_{\rm max}} \frac{d\theta_{\rm cm}}{\sin\theta_{\rm cm}} \int dk \frac{d^3N_\gamma}{dkd^2b} \int \frac{dx_2}{x_2} \times \Big[\sum_{i=q,\overline{q}} F_i^A(x_2, \mu^2, \vec{b}, z) \frac{d\sigma_{\gamma i \rightarrow \gamma i}}{dt} \frac{D_{h/i}(z_c, \mu^2)}{z_c} \Big] \quad (12)$$

where X on the left-hand side includes the final-state gluon. On the partonic level, both the initial and final state partons are identical so that parton i fragments into hadron h according to the fragmentation function, $D_{h/i}(z_c, \mu^2)$. The subprocess cross sections, $d\sigma/dt$, are related to $s^2 d\sigma/dtdu$ in Eq. (10) through the momentum-conserving delta function $\delta(s+t+u)$ and division by s^2. Our results, shown in Fig. 15, are presented in the interval $|y_1| \leq 1$.

The cross section for γ+hadron production are, again, several orders of magnitude lower than the dijet calculations shown in Fig. 6(a). At the values of z_c and x important for dijet production, the final state is dominated by quarks and antiquarks which fragment more frequently into charged hadrons than do gluons. While $\gamma g \to q\overline{q}$ produces quarks and antiquarks with identical distributions, the contribution from the $\gamma q \to qg$ channel makes *e.g.* pion production by quarks and antiquarks asymmetric. We also note that for $p_T < 100$ GeV, 60% of the dijet final state particles are pions, $\approx 33\%$ kaons and $\approx 7\%$ protons. As p_T increases, the pion and proton contributions decrease slightly while the kaon fraction increases. In the case of γ+hadron final states, there is no initial state gluon channel. Thus the valence quarks dominate hadron production and the relative fraction of produced pions increases to 66%. The kaon and proton fractions are subsequently decreased to $\approx 28\%$ and $\approx 6\%$ respectively.

The shadowing ratios, shown in Fig. 15(b) and (c) for produced pions, kaons and protons separately for Pb+Pb as well as the total ratios for Ar+Ar and O+O collisions, reflect the quark-initiated processes. We show the results for all charged hadrons here since we do not differentiate between quark and antiquark production. The ratios, almost identical for produced pions, kaons and charged hadrons, are quite different from the ratios shown for pion production by quarks and antiquarks in Fig. 6(c) and (d) since these pions originate from initial-state gluons and thus exhibit antishadowing. The results are similar to pions from gluon jets in Fig. 6. However, in this case the ratios are slightly higher due to the relative couplings. The proton ratios are lower than those for pions and kaons due to the nuclear isospin. The dominance of d valence quarks in nuclei reduces the proton production rate since d quarks are only half as effective at producing protons as u quarks in the KKP fragmentation scheme [33]. This lower weight in the final state reduces the effectiveness of proton production by the initial state, decreasing the produced proton shadowing ratios relative to pions and kaons. Valence quarks dominate the observed final state shadowing at these larger values of x, as in Fig. 7.

C. Resolved γ+jet production

Now we turn to resolved production of γ+jet final states. The resolved jet photoproduction cross section for partons of flavor f in the subprocess $ij \to k\gamma$ in AB collisions is modified from Eq. (8) so that now

$$\begin{aligned} S^2_{NN} \frac{d\sigma^{\rm res}_{\gamma A \to \gamma + {\rm jet} X}}{dTdUd^2b} &= 2\int dz \int_{k_{\rm min}}^{\infty} \frac{dk}{k} \frac{d^3N_\gamma}{dkd^2b} \int_{k_{\rm min}/k}^{1} \frac{dx}{x} \int_{x_{2_{\rm min}}}^{1} \frac{dx_2}{x_2} \\ &\times \sum_{\substack{ij= \\ \langle kl \rangle}} \left\{ F_i^\gamma(x,\mu^2) F_j^A(x_2,\mu^2,\vec{b},z) + F_j^\gamma(x,\mu^2) F_i^A(x_2,\mu^2,\vec{b},z) \right\} \\ &\times \delta_{fk} \left[\hat{s}^2 \frac{d\sigma^{ij\to k\gamma}}{d\hat{t}d\hat{u}}(\hat{t},\hat{u}) + \hat{s}^2 \frac{d\sigma^{ij\to k\gamma}}{d\hat{t}d\hat{u}}(\hat{u},\hat{t}) \right] \ . \end{aligned} \qquad (13)$$

The resolved diagrams are those for hadroproduction of direct photons, $qg \to q\gamma$ and $q\overline{q} \to g\gamma$. The $2 \to 2$ minijet subprocess cross sections are [39]

$$\hat{s}^2 \frac{d^2\sigma_{qg}}{d\hat{t}d\hat{u}} = -\frac{1}{3}\pi\alpha_s\alpha e_Q^2 \left[\frac{\hat{s}^2+\hat{u}^2}{\hat{s}\hat{u}}\right]\delta(\hat{s}+\hat{t}+\hat{u}) \tag{14}$$

$$\hat{s}^2 \frac{d^2\sigma_{q\overline{q}}}{d\hat{t}d\hat{u}} = \frac{8}{9}\pi\alpha_s\alpha e_Q^2 \left[\frac{\hat{t}^2+\hat{u}^2}{\hat{t}\hat{u}}\right]\delta(\hat{s}+\hat{t}+\hat{u}) \ . \tag{15}$$

Note that there is no factor $1/(1+\delta_{kl})$, as in Eq. (8), since there are no identical particles in the final state.

The resolved γ+jet results are shown in Fig. 16 using the GRV LO photon parton densities. Along with the total partonic rates in Pb+Pb collisions, we also show the individual partonic contributions to the jet p_T distributions in Fig. 16(a). The total yields are slightly higher for the resolved than the direct contribution where only one channel is open and the coupling is smaller. Quark and antiquark production by the qg process is dominant for $p_T < 40$ GeV but, at higher p_T, gluon production dominates from the $q\overline{q}$ channel. The large values of x again makes the valence quark contribution dominant at higher p_T. The total p_T distributions for Ar+Ar and O+O collisions are also shown.

The strong antishadowing in the produced quark and antiquark ratios in Fig. 16(b) and (c) comes from the qg channel. The antiquark ratio is higher because the qg parton luminosity peaks at higher x than the $\overline{q}g$ luminosity and at lower x the gluon antishadowing ratio is larger. The difference between the quark and antiquark ratios increases with p_T since the average x and thus the valence quark contribution also grow with p_T. At high p_T, the flattening of the FGS quark and antiquark ratios is due to the flattening of the gluon parameterization at $x > 0.2$.

The final-state gluon ratio shows little antishadowing since it arises from the $q\overline{q}$ channel. The antishadowing in the EKS98 ratio is due to the valence quarks while the higher ratio for FGS reflects the fact that the antiquark ratios also show antishadowing for $x < 0.2$. The ratio for the total is essentially the average of the three contributions at low p_T, where they are similar, while at high p_T, where the $q\overline{q}$ channel dominates, the total ratio approximates the produced gluon ratio in both cases.

The resolved rapidity distributions are also shown in Fig. 13 for the two p_T cuts. The resolved distribution is not as broad at negative y_1 as that of the dijet process in Fig. 4 due to the smaller relative gluon contribution and the reduced number of channels available for the γ+jet process. Note that the relative resolved to direct production is reduced here and the direct process is actually dominant at $y_1 > 0$ for $p_T > 10$ GeV and for all y_1 at $p_T > 100$ GeV. The antishadowing peak is higher for resolved production, shown in Fig. 14, thanks to the gluon contribution to resolved production.

Finally, we show the resolved to direct ratio in Fig. 17. The direct rate alone should be observable at $y_1 > -4$ for Pb+Pb, $y_1 \sim -2.5$ for Ar+Ar and $y_1 \sim 0$ for O+O and $p_T > 10$ GeV. Direct production dominates over all y_1 by a large factor when $p_T > 100$ GeV. Although the rates are lower than the dijet rates, the dominance of direct γ+jet production implies than the nuclear quark distribution can be cleanly studied.

The resolved γ+jet rates are shown in Table V. These rates are only slightly larger than the direct rates for $p_T \leq 20$ GeV but drop below the direct rates at higher p_T since there is no large growth in the number of available production channels, as in dijet production. In addition, the lower effective energy plays an important role here as well.

D. Resolved γ+hadron production

The leading particle p_T distributions of jets from γ+jet production are

$$\begin{aligned}\frac{d\sigma^{\rm res}_{\gamma A\to\gamma+hX}}{dp_T d^2b} &= 4p_T \int dz \int_{\theta_{\rm min}}^{\theta_{\rm max}} \frac{d\theta_{\rm cm}}{\sin\theta_{\rm cm}} \int_{k_{\rm min}}^{\infty} \frac{dk}{k}\frac{d^3N_\gamma}{dkd^2b}\int_{k_{\rm min}/k}^{1} \frac{dx}{x}\int_{x_{2_{\rm min}}}^{1} \frac{dx_2}{x_2} \\ &\times \sum_{\substack{ij= \\ \langle kl\rangle}} \left\{F_i^\gamma(x,\mu^2)F_j^A(x_2,\mu^2,\vec{b},z) + F_j^\gamma(x,\mu^2)F_i^A(x_2,\mu^2,\vec{b},z)\right\} \\ &\times \delta_{fk}\left[\frac{d\sigma}{d\hat{t}}^{ij\to k\gamma}(\hat{t},\hat{u}) + \frac{d\sigma}{d\hat{t}}^{ij\to k\gamma}(\hat{u},\hat{t})\right]\frac{D_{h/k}(z_c,\mu^2)}{z_c}\ . \end{aligned} \tag{16}$$

The subprocess cross sections, $d\sigma/d\hat{t}$, are related to $\hat{s}^2 d\sigma/d\hat{t}d\hat{u}$ in Eq. (13) through the momentum-conserving delta function $\delta(\hat{s}+\hat{t}+\hat{u})$ and division by $\hat{s}^2$.

The resolved p_T distributions for hadrons are shown in Fig. 18(a). Note that the resolved cross section for leading hadron production is similar to direct production, shown in Fig. 15(a). The same effect is seen for dijet production in Figs. 10 and 6.

The shadowing ratios are shown in Fig. 18. The difference between the shadowing ratios for pions produced by quarks and antiquarks is rather large and reflects both gluon antishadowing at low p_T as well as the relative valence to sea contributions for quark and antiquark production through $q(\overline{q})g \to q(\overline{q})\gamma$. In the FGS calculations, the antiquark ratio reflects the flattening of the antiquark and gluon ratios at $x > 0.2$. Since pions produced by gluons come from the $q\overline{q} \to \gamma g$ channel alone, only a small effect is seen, primarily in the EMC region. Now the total pion rates follow those for quark and antiquark production of final-state pions instead of those of the gluon.

Although our p_T-dependent calculations have focused on the midrapidity region of $|y_1| \leq 1$, we have shown that extending the rapidity coverage could lead to greater sensitivity to the small x_2 region and larger contributions from direct photoproduction, especially at low p_T.

Thus γ+jet production is a good way to measure the nuclear quark distribution functions. Direct photoproduction is dominant at central rapidities for moderate values of p_T. Final-state hadron production is somewhat larger for direct production so that, even if the rates are low, the results will be relatively clean.

IV. SUMMARY

There are a number of uncertainties in our results. All our calculations are at leading order so that there is some uncertainty in the total rate, see Refs. [9,40]. Some uncertainty also arises from the scale dependence, both in the parton densities and in the fragmentation functions. The fragmentation functions at large z_c also introduce uncontrollable uncertainties in the rates. Hopefully more data will bring the parton densities in the photon, proton and nucleus under better control before the LHC begins operation. The data from RHIC also promises to bring the fragmentation functions under better control in the near future.

While the photon flux is also an uncertainty, it can be determined experimentally. The hadronic interaction probability near the minimum radius depends on the matter distribution in the nucleus. Our calculations use Woods-Saxon distributions with parameters fit to electron scattering data. This data is quite accurate. However, electron scattering is only sensitive to the charge distribution in the nucleus. Recent measurements indicate that the neutron and proton distributions differ in nuclei [41]. This uncertainty in the matter distribution is likely to limit the photon flux determination.

The uncertainty in the photon flux can be reduced by calibrating it with other measurements such as vector meson production, $\gamma A \rightarrow VA$. Studies of well known two-photon processes, like lepton production, can also help refine the determination of the photon flux. With such checks, it should be possible to understand the photon flux in pA relative to AA to better than 10%, good enough for a useful shadowing measurement.

We would like to thank S. R. Klein and M. Strikman for discussions. This work was supported in part by the Division of Nuclear Physics of the Office of High Energy and Nuclear Physics of the U.S. Department of Energy under Contract No. DE-AC-03-76SF00098.

REFERENCES

[1] E. Witten, Nucl. Phys. B **120** (1977) 189.

[2] T. Sjöstrand, J. K. Storrow, and A. Vogt, J. Phys. G **22** (1996) 893 [arXiv:hep-ph/9601351].

[3] C. Adler *et al.* [STAR Collaboration], Phys. Rev. Lett. **90** (2003) 082302 [arXiv:nucl-ex/0210033].

[4] M. Chiu [PHENIX Collaboration], Nucl. Phys. A **715** (2003) 761 [arXiv:nucl-ex/0211008].

[5] K. J. Eskola and X. N. Wang, Int. J. Mod. Phys. A **10** (1995) 3071.

[6] V. Emel'yanov, A. Khodinov, S. R. Klein and R. Vogt, Phys. Rev. C **61** (2000) 044904 [arXiv:hep-ph/9909427].

[7] K. J. Eskola, K. Kajantie and J. Lindfors, Nucl. Phys. B **323** (1989) 37.

[8] K. J. Eskola and K. Kajantie, Z. Phys. C **75** (1997) 515 [arXiv:nucl-th/9610015].

[9] S. R. Klein, J. Nystrand and R. Vogt, Phys. Rev. C **66** (2002) 044906 [arXiv:hep-ph/0206220].

[10] J. Smith and W. L. van Neerven, Nucl. Phys. B **374** (1992) 36.

[11] S. Klein and J. Nystrand, Phys. Rev. C **60** (1999) 014903 [arXiv:hep-ph/9902259].

[12] V. Emel'yanov, A. Khodinov, S. R. Klein and R. Vogt, Phys. Rev. C **56** (1997) 2726 [arXiv:nucl-th/9706085].

[13] V. Emel'yanov, A. Khodinov, S. R. Klein and R. Vogt, Phys. Rev. Lett. **81** (1998) 1801 [arXiv:nucl-th/9805027].

[14] V. Emel'yanov, A. Khodinov, S. R. Klein, and R. Vogt, Phys. Rev. C **59** (1999) 1860 [arXiv:hep-ph/9809222].

[15] R. Vogt, Phys. Rev. C **64** (2001) 044901 [arXiv:hep-ph/0011242].

[16] A. D. Martin, R. G. Roberts, W. J. Stirling and R. S. Thorne, Phys. Lett. B **443** 301 (1998) [arXiv:hep-ph/9808371].

[17] C. W. De Jager, H. De Vries and C. De Vries, Atom. Data Nucl. Data Tabl. **14** (1974) 479.

[18] M. Gluck, E. Reya and A. Vogt, Z. Phys. C **53** (1992) 127.

[19] K. J. Eskola, V. J. Kolhinen and P. V. Ruuskanen, Nucl. Phys. B **535** (1998) 351 [arXiv:hep-ph/9802350].

[20] K. J. Eskola, V. J. Kolhinen and C. A. Salgado, Eur. Phys. J. C **9** (1999) 61 [arXiv:hep-ph/9807297].

[21] L. Frankfurt, V. Guzey and M. Strikman, arXiv:hep-ph/0303022.

[22] H. L. Lai *et al.* [CTEQ Collaboration], Eur. Phys. J. C **12** (2000) 375 [arXiv:hep-ph/9903282].

[23] M. Glück, E. Reya, and A. Vogt, Phys. Rev. D **46** (1992) 1973.

[24] M. Glück, E. Reya, and A. Vogt, Phys. Rev. D **45** (1992) 3986.

[25] M. Drees and K. Grassie, Z. Phys. C **28** (1985) 451.

[26] H. Abramowicz, K. Charchula, and A. Levy, Phys. Lett. B **269** (1991) 458.

[27] K. Hagiwara, M. Tanaka, I. Watanabe, and T. Izubuchi, Phys. Rev. D **51** (1995) 3197 [arXiv:hep-ph/9406252].

[28] G. A. Schuler and T. Sjöstrand, Z. Phys. C **68** (1995) 607 [arXiv:hep-ph/9503384].

[29] G. A. Schuler and T. Sjöstrand, Phys. Lett. B **376** (1996) 193 [arXiv:hep-ph/9601282].

[30] H. Plothow-Besch, 'PDFLIB: Proton, Pion and Photon Parton Density Functions, Par-

ton Density Functions of the Nucleus, and α_s Calculations', User's Manual - Version 8.04, W5051 PDFLIB, 2000.04.17, CERN-ETT/TT.

[31] W. Bartel *et al.* [JADE Collaboration], Z. Phys. C **24** (1984) 231.

[32] R. D. Field, *Applications Of Perturbative QCD* (Addison-Wesley, Redwood City, CA, 1989).

[33] B. A. Kniehl, G. Kramer and B. Pötter, Nucl. Phys. B **582** (2000) 514 [arXiv:hep-ph/0010289].

[34] B. A. Kniehl, G. Kramer and B. Pötter, Nucl. Phys. B **597** (2001) 337 [arXiv:hep-ph/0011155].

[35] X. f. Zhang, G. Fai and P. Lévai, Phys. Rev. Lett. **89** (2002) 272301 [arXiv:hep-ph/0205008].

[36] M. Gyulassy, P. Levai and I. Vitev, Phys. Lett. B **538** (2002) 282 [arXiv:nucl-th/0112071].

[37] I. Vitev, M. Gyulassy and P. Levai, arXiv:nucl-th/0204019.

[38] T. Sakaguchi [PHENIX Collaboration], Nucl. Phys. A **715** (2003) 757 [arXiv:nucl-ex/0209030].

[39] J. F. Owens, Rev. Mod. Phys. **59** (1987) 465.

[40] R. Vogt, Heavy Ion Phys. **17** (2003) 75 [arXiv:hep-ph/0207359].

[41] A. Trzcinska, J. Jastrzebski, P. Lubinski, F. J. Hartmann, R. Schmidt, T. von Egidy and B. Klos, Phys. Rev. Lett. **87** (2001) 082501.

TABLES

A	L (mb^{-1}s^{-1})	$\sqrt{S_{NN}}$ (GeV)	$E_{\rm beam}$ (GeV)	γ_L	$k_{\rm max}$ (GeV)	$E_{\rm max}$ (TeV)	$\sqrt{S_{\gamma N}}$ (GeV)
O	160	7000	3500	3730	243	1820	1850
Ar	43	6300	3150	3360	161	1080	1430
Pb	0.42	5500	2750	2930	81	480	950

TABLE I. Pertinent parameters and kinematic limits for AA collisions at the LHC [9]. We first give the luminosities and the NN collision kinematics, the nucleon-nucleon center of mass energies, $\sqrt{S_{NN}}$, the corresponding beam energies, $E_{\rm beam}$, Lorentz factors, γ_L. We then present the photon cutoff energies in the center of mass frame, $k_{\rm max}$, and in the nuclear rest frame, $E_{\rm max}$, as well as the equivalent maximum photon-nucleon center of mass energies, $\sqrt{S_{\gamma N}}$.

	Pb+Pb		Ar+Ar		O+O	
p_T (GeV)	$d\sigma/dp_T$	Rate	$d\sigma/dp_T$	Rate	$d\sigma/dp_T$	Rate
11.4	2.802×10^{5}	1.177×10^{5}	4.771×10^{3}	2.052×10^{5}	5.506×10^{2}	8.810×10^{4}
21.4	1.389×10^{4}	5.836×10^{3}	2.869×10^{2}	1.234×10^{4}	3.706×10^{1}	5.930×10^{3}
31.4	1.907×10^{3}	8.010×10^{2}	4.574×10^{1}	1.967×10^{3}	6.462×10^{0}	1.034×10^{3}
41.4	4.181×10^{2}	1.756×10^{2}	1.137×10^{1}	4.889×10^{2}	1.734×10^{0}	2.774×10^{2}
51.4	1.207×10^{2}	5.069×10^{1}	3.668×10^{0}	1.577×10^{2}	5.983×10^{-1}	9.573×10^{1}
61.4	4.172×10^{1}	1.752×10^{1}	1.403×10^{0}	6.033×10^{1}	2.434×10^{-1}	3.894×10^{1}
71.4	1.640×10^{1}	6.890×10^{0}	6.061×10^{-1}	2.606×10^{1}	1.113×10^{-1}	1.781×10^{1}
81.4	7.105×10^{0}	2.984×10^{0}	2.868×10^{-1}	1.233×10^{1}	5.557×10^{-2}	8.891×10^{0}
91.4	3.316×10^{0}	1.393×10^{0}	1.457×10^{-1}	6.265×10^{0}	2.970×10^{-2}	4.752×10^{0}
101	1.640×10^{0}	6.888×10^{-1}	7.832×10^{-2}	3.368×10^{0}	1.676×10^{-2}	2.682×10^{0}
111	8.538×10^{-1}	3.586×10^{-1}	4.416×10^{-2}	1.899×10^{0}	9.898×10^{-3}	1.584×10^{0}
121	4.624×10^{-1}	1.942×10^{-1}	2.586×10^{-2}	1.112×10^{0}	6.066×10^{-3}	9.706×10^{-1}
131	2.588×10^{-1}	1.087×10^{-1}	1.564×10^{-2}	6.725×10^{-1}	3.835×10^{-3}	6.136×10^{-1}
141	1.493×10^{-1}	6.270×10^{-2}	9.737×10^{-3}	4.187×10^{-1}	2.493×10^{-3}	3.989×10^{-1}
151	8.838×10^{-2}	3.712×10^{-2}	6.215×10^{-3}	2.672×10^{-1}	1.660×10^{-3}	2.656×10^{-1}
161	5.346×10^{-2}	2.245×10^{-2}	4.050×10^{-3}	1.741×10^{-1}	1.128×10^{-3}	1.805×10^{-1}
171	3.293×10^{-2}	1.383×10^{-2}	2.687×10^{-3}	1.155×10^{-1}	7.803×10^{-4}	1.248×10^{-1}
181	2.064×10^{-2}	8.669×10^{-3}	1.813×10^{-3}	7.796×10^{-2}	5.485×10^{-4}	8.776×10^{-2}
191	1.316×10^{-2}	5.528×10^{-3}	1.244×10^{-3}	5.349×10^{-2}	3.917×10^{-4}	6.267×10^{-2}
201	8.507×10^{-3}	3.573×10^{-3}	8.642×10^{-4}	3.716×10^{-2}	2.833×10^{-4}	4.533×10^{-2}

TABLE II. The differential cross sections, in units of nb/GeV, without shadowing and rates for $|y_1| \leq 1$ in a one month, 10^6 s, run for direct dijet photoproduction in peripheral AA collisions.

	Pb+Pb		Ar+Ar		O+O	
p_T (GeV)	$d\sigma/dp_T$	Rate	$d\sigma/dp_T$	Rate	$d\sigma/dp_T$	Rate
11.4	5.184×10^{5}	2.177×10^{5}	1.185×10^{4}	5.096×10^{5}	1.747×10^{3}	2.795×10^{5}
21.4	1.733×10^{4}	7.279×10^{3}	4.713×10^{2}	2.027×10^{4}	7.715×10^{1}	1.234×10^{4}
31.4	1.895×10^{3}	7.959×10^{2}	5.927×10^{1}	2.549×10^{3}	1.054×10^{1}	1.686×10^{3}
41.4	3.530×10^{2}	1.483×10^{2}	1.247×10^{1}	5.362×10^{2}	2.386×10^{0}	3.818×10^{2}
51.4	8.945×10^{1}	3.757×10^{1}	3.530×10^{0}	1.518×10^{2}	7.210×10^{-1}	1.154×10^{2}
61.4	2.767×10^{1}	1.162×10^{1}	1.210×10^{0}	5.203×10^{1}	2.629×10^{-1}	4.206×10^{1}
71.4	9.857×10^{0}	4.140×10^{0}	4.754×10^{-1}	2.044×10^{1}	1.094×10^{-1}	1.750×10^{1}
81.4	3.905×10^{0}	1.640×10^{0}	2.068×10^{-1}	8.892×10^{0}	5.031×10^{-2}	8.050×10^{0}
91.4	1.679×10^{0}	7.052×10^{-1}	9.726×10^{-2}	4.182×10^{0}	2.496×10^{-2}	3.994×10^{0}
101	7.687×10^{-1}	3.229×10^{-1}	4.864×10^{-2}	2.092×10^{0}	1.315×10^{-2}	2.104×10^{0}
111	3.725×10^{-1}	1.565×10^{-1}	2.566×10^{-2}	1.103×10^{0}	7.296×10^{-3}	1.167×10^{0}
121	1.884×10^{-1}	7.913×10^{-2}	1.411×10^{-2}	6.067×10^{-1}	4.215×10^{-3}	6.744×10^{-1}
131	9.870×10^{-2}	4.145×10^{-2}	8.036×10^{-3}	3.455×10^{-1}	2.519×10^{-3}	4.030×10^{-1}
141	5.353×10^{-2}	2.248×10^{-2}	4.728×10^{-3}	2.033×10^{-1}	1.554×10^{-3}	2.486×10^{-1}
151	2.986×10^{-2}	1.254×10^{-2}	2.858×10^{-3}	1.229×10^{-1}	9.840×10^{-4}	1.574×10^{-1}
161	1.704×10^{-2}	7.157×10^{-3}	1.767×10^{-3}	7.598×10^{-2}	6.372×10^{-4}	1.020×10^{-1}
171	9.929×10^{-3}	4.170×10^{-3}	1.115×10^{-3}	4.795×10^{-2}	4.207×10^{-4}	6.731×10^{-2}
181	5.895×10^{-3}	2.476×10^{-3}	7.159×10^{-4}	3.078×10^{-2}	2.827×10^{-4}	4.523×10^{-2}
191	3.569×10^{-3}	1.499×10^{-3}	4.685×10^{-4}	2.015×10^{-2}	1.935×10^{-4}	3.096×10^{-2}
201	2.192×10^{-3}	9.206×10^{-4}	3.110×10^{-4}	1.337×10^{-2}	1.342×10^{-4}	2.147×10^{-2}

TABLE III. The differential cross sections, in units of nb/GeV, without shadowing and rates with $|y_1| \leq 1$ in a one month, 10^6 s, run for resolved dijet photoproduction in peripheral AA collisions.

	Pb+Pb		Ar+Ar		O+O	
p_T (GeV)	$d\sigma/dp_T$	Rate	$d\sigma/dp_T$	Rate	$d\sigma/dp_T$	Rate
11.4	1.877×10^{2}	7.886×10^{1}	2.838×10^{0}	1.220×10^{1}	3.024×10^{-1}	4.838×10^{1}
21.4	1.435×10^{1}	6.026×10^{0}	2.534×10^{-1}	1.090×10^{1}	2.948×10^{-2}	4.716×10^{0}
31.4	1.656×10^{0}	1.116×10^{0}	5.310×10^{-2}	2.284×10^{0}	6.630×10^{-3}	1.061×10^{0}
41.4	7.326×10^{-1}	3.076×10^{-1}	1.633×10^{-2}	7.022×10^{-1}	2.168×10^{-3}	3.468×10^{-1}
51.4	2.546×10^{-1}	1.069×10^{-1}	6.264×10^{-3}	2.694×10^{-1}	8.804×10^{-4}	1.408×10^{-1}
61.4	1.027×10^{-1}	4.314×10^{-2}	2.778×10^{-3}	1.195×10^{-1}	4.116×10^{-4}	6.586×10^{-2}
71.4	4.602×10^{-2}	1.933×10^{-2}	1.362×10^{-3}	5.856×10^{-2}	2.124×10^{-4}	3.400×10^{-2}
81.4	2.228×10^{-2}	9.358×10^{-3}	7.200×10^{-4}	3.096×10^{-2}	1.179×10^{-4}	1.887×10^{-2}
91.4	1.146×10^{-2}	4.814×10^{-3}	4.034×10^{-4}	1.735×10^{-2}	6.930×10^{-5}	1.109×10^{-2}
101	6.176×10^{-3}	2.594×10^{-3}	2.366×10^{-4}	1.017×10^{-2}	4.258×10^{-5}	6.812×10^{-3}
111	3.464×10^{-3}	1.455×10^{-3}	1.441×10^{-4}	6.196×10^{-3}	2.716×10^{-5}	4.346×10^{-3}
121	2.006×10^{-3}	8.426×10^{-4}	9.052×10^{-5}	3.892×10^{-3}	1.785×10^{-5}	2.856×10^{-3}
131	1.192×10^{-3}	5.004×10^{-4}	5.832×10^{-5}	2.508×10^{-3}	1.203×10^{-5}	1.924×10^{-3}
141	7.254×10^{-4}	3.046×10^{-4}	3.846×10^{-5}	1.654×10^{-3}	8.292×10^{-6}	1.327×10^{-3}
151	4.506×10^{-4}	1.893×10^{-4}	2.586×10^{-5}	1.112×10^{-3}	5.826×10^{-6}	9.322×10^{-4}
161	2.848×10^{-4}	1.196×10^{-4}	1.769×10^{-5}	7.604×10^{-4}	4.160×10^{-6}	6.656×10^{-4}
171	1.825×10^{-4}	7.666×10^{-5}	1.227×10^{-5}	5.274×10^{-4}	3.014×10^{-6}	4.822×10^{-4}
181	1.186×10^{-4}	4.982×10^{-5}	8.620×10^{-6}	3.706×10^{-4}	2.210×10^{-6}	3.536×10^{-4}
191	7.816×10^{-5}	3.282×10^{-5}	6.134×10^{-6}	2.638×10^{-4}	1.642×10^{-6}	2.628×10^{-4}
201	5.204×10^{-5}	2.186×10^{-5}	4.412×10^{-6}	1.897×10^{-4}	1.233×10^{-6}	1.972×10^{-4}

TABLE IV. The differential cross sections, in units of nb/GeV, without shadowing and rates in the interval $|y_1| \leq 1$ in a one month, 10^6 s, run for direct γ+jet photoproduction in peripheral AA collisions.

	Pb+Pb		Ar+Ar		O+O	
p_T (GeV)	$d\sigma/dp_T$	Rate	$d\sigma/dp_T$	Rate	$d\sigma/dp_T$	Rate
11.4	1.154×10^{2}	4.847×10^{1}	2.456×10^{0}	1.056×10^{2}	3.333×10^{-1}	5.333×10^{1}
21.4	5.352×10^{0}	2.248×10^{0}	1.391×10^{-1}	5.981×10^{0}	2.137×10^{-2}	3.419×10^{0}
31.4	7.037×10^{-1}	2.956×10^{-1}	2.126×10^{-2}	9.142×10^{-1}	3.588×10^{-3}	5.741×10^{-1}
41.4	1.497×10^{-1}	6.287×10^{-2}	5.123×10^{-3}	2.203×10^{-1}	9.352×10^{-4}	1.496×10^{-1}
51.4	4.216×10^{-2}	1.771×10^{-2}	1.611×10^{-3}	6.927×10^{-2}	3.151×10^{-4}	5.042×10^{-2}
61.4	1.427×10^{-2}	5.993×10^{-3}	6.037×10^{-4}	2.596×10^{-2}	1.257×10^{-4}	2.011×10^{-2}
71.4	5.502×10^{-3}	2.311×10^{-3}	2.561×10^{-4}	1.101×10^{-2}	5.647×10^{-5}	9.035×10^{-3}
81.4	2.338×10^{-3}	9.820×10^{-4}	1.192×10^{-4}	5.126×10^{-3}	2.776×10^{-5}	4.442×10^{-3}
91.4	1.071×10^{-3}	4.498×10^{-4}	5.962×10^{-5}	2.564×10^{-3}	1.463×10^{-5}	2.341×10^{-3}
101	5.198×10^{-4}	2.183×10^{-4}	3.155×10^{-5}	1.357×10^{-3}	8.144×10^{-6}	1.303×10^{-3}
111	2.655×10^{-4}	1.115×10^{-4}	1.752×10^{-5}	7.534×10^{-4}	4.749×10^{-6}	7.598×10^{-4}
121	1.410×10^{-4}	5.922×10^{-5}	1.011×10^{-5}	4.347×10^{-4}	2.875×10^{-6}	4.600×10^{-4}
131	7.736×10^{-5}	3.249×10^{-5}	6.025×10^{-6}	2.591×10^{-4}	1.795×10^{-6}	2.872×10^{-4}
141	4.376×10^{-5}	1.838×10^{-5}	3.696×10^{-6}	1.589×10^{-4}	1.153×10^{-6}	1.845×10^{-4}
151	2.539×10^{-5}	1.066×10^{-5}	2.323×10^{-6}	9.989×10^{-5}	7.589×10^{-7}	1.214×10^{-4}
161	1.505×10^{-5}	6.321×10^{-6}	1.491×10^{-6}	6.411×10^{-5}	5.095×10^{-7}	8.152×10^{-5}
171	9.078×10^{-6}	3.813×10^{-6}	9.743×10^{-7}	4.189×10^{-5}	3.482×10^{-7}	5.571×10^{-5}
181	5.571×10^{-6}	2.340×10^{-6}	6.471×10^{-7}	2.783×10^{-5}	2.419×10^{-7}	3.870×10^{-5}
191	3.478×10^{-6}	1.461×10^{-6}	4.369×10^{-7}	1.879×10^{-5}	1.707×10^{-7}	2.731×10^{-5}
201	2.200×10^{-6}	9.240×10^{-7}	2.988×10^{-7}	1.285×10^{-5}	1.220×10^{-7}	1.952×10^{-5}

TABLE V. The differential cross sections, in units of nb/GeV, without shadowing and rates in the interval $|y_1| \leq 1$ in a one month, 10^6 s, run for resolved γ+jet photoproduction in peripheral AA collisions.

FIGURES

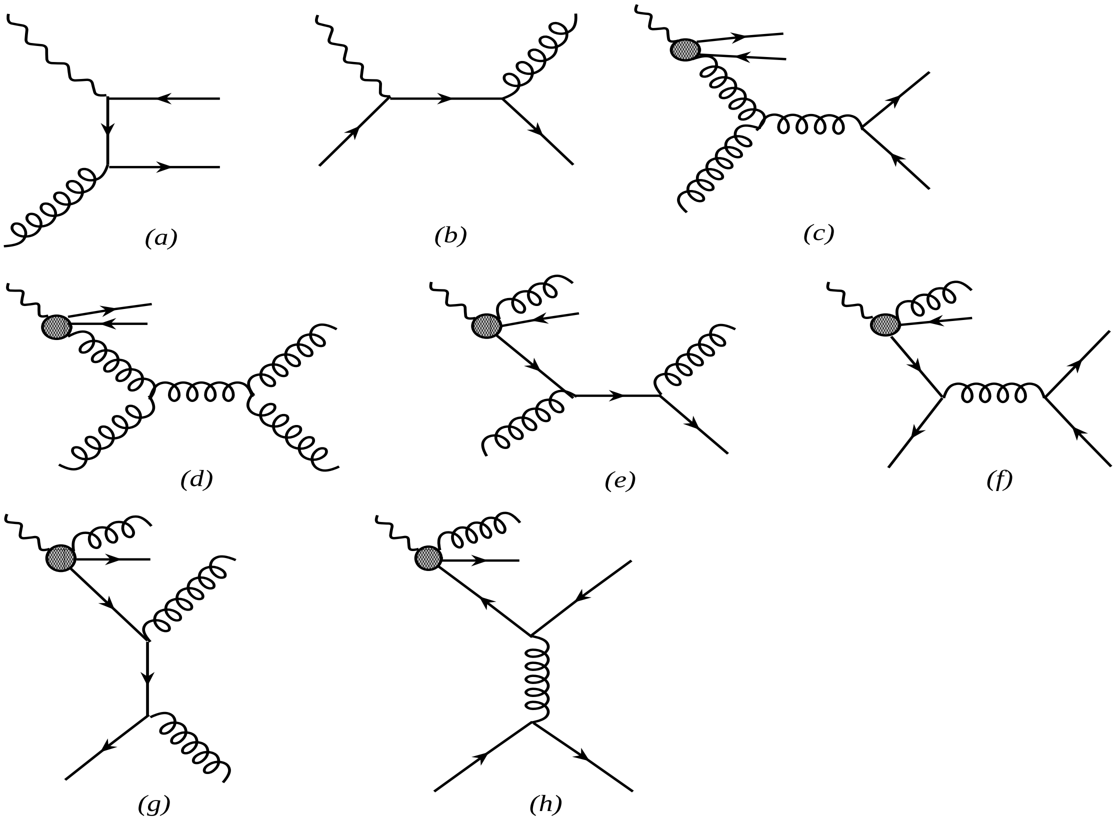

FIG. 1. Feynman diagrams for dijet photoproduction from direct, (a) and (b), and resolved photons, (c)-(h). Only a sample of the resolved diagrams are shown. Crossed diagrams are not shown.

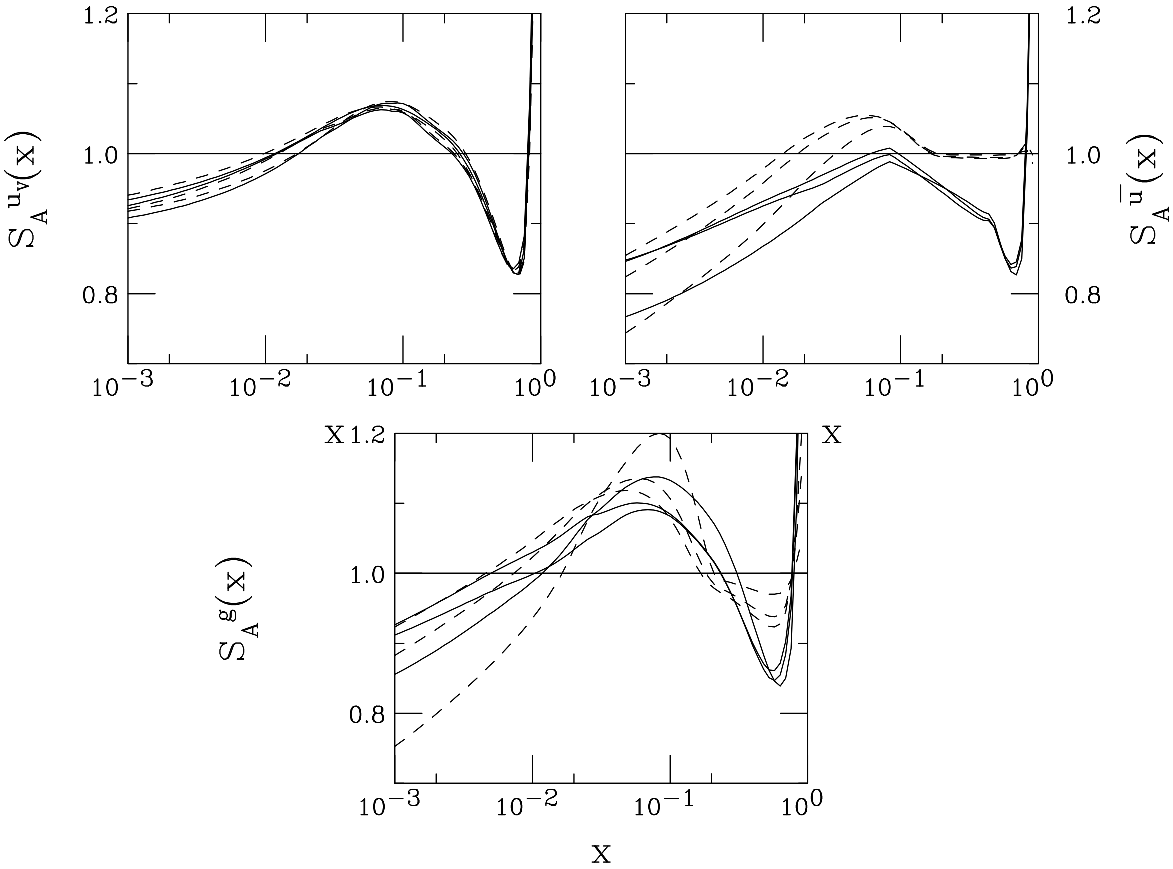

FIG. 2. The EKS98 and FGS shadowing parameterizations are compared at the scale $\mu = 10$, 100 and 400 GeV for (a) valence quarks, (b) sea quarks and (c) gluons. The solid curves are the EKS98 parameterization, the dashed, FGS. The lower values of μ give the lowest values of S_A^i.

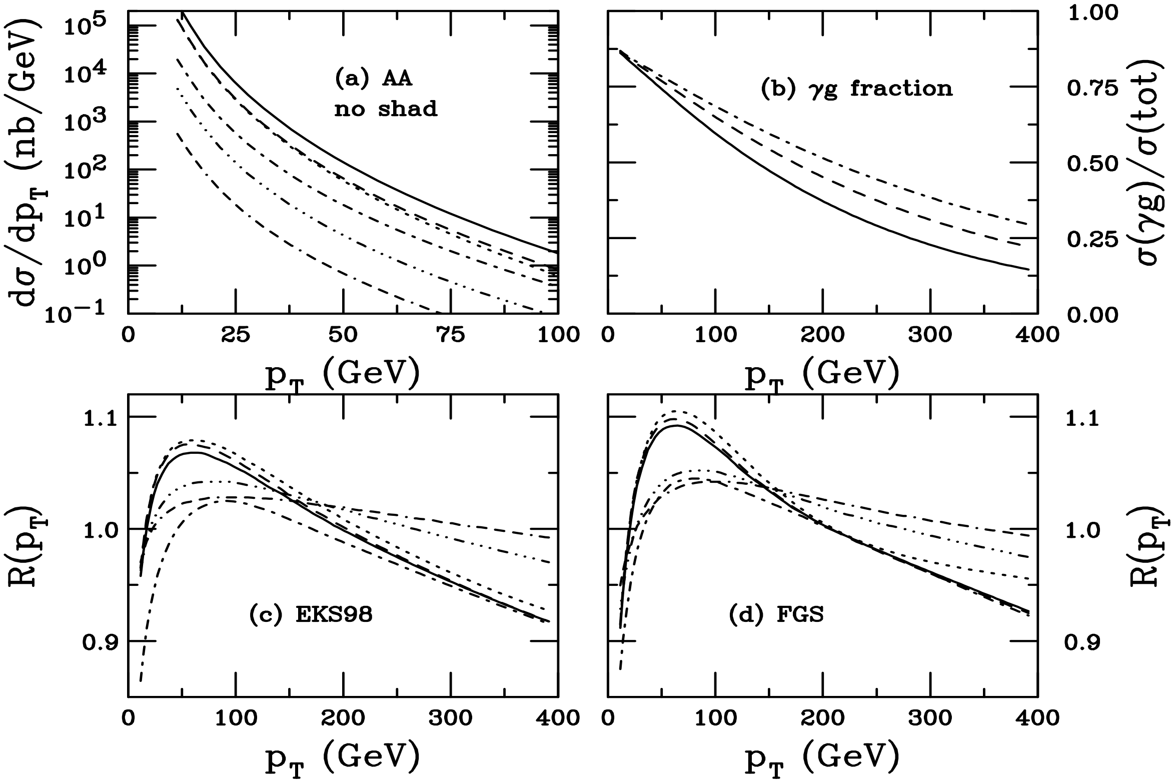

FIG. 3. Direct jet photoproduction in peripheral collisions. (a) The p_T distributions for $|y_1| \leq 1$ are shown for AA collisions. The solid curves is the total for Pb ions while the produced quarks (dashed), antiquarks (dotted) and gluons (dot-dashed) are shown separately. The total production for Ar (dot-dot-dot-dashed) and O (dot-dash-dash-dashed) ions are also shown. (b) The fraction of gluon-initiated jets as a function of p_T for Pb+Pb (solid), Ar+Ar (dashed) and O+O (dot-dashed) interactions. (c) The EKS98 shadowing ratios for produced partons. The solid curve is the total for Pb ions while the ratios for produced quarks (dashed), antiquarks (dotted) and gluons (dot-dashed) are shown separately. The total ratios for Ar (dot-dot-dot-dashed) and O (dot-dash-dash-dashed) ions are also shown. (d) The same as (c) for FGS.

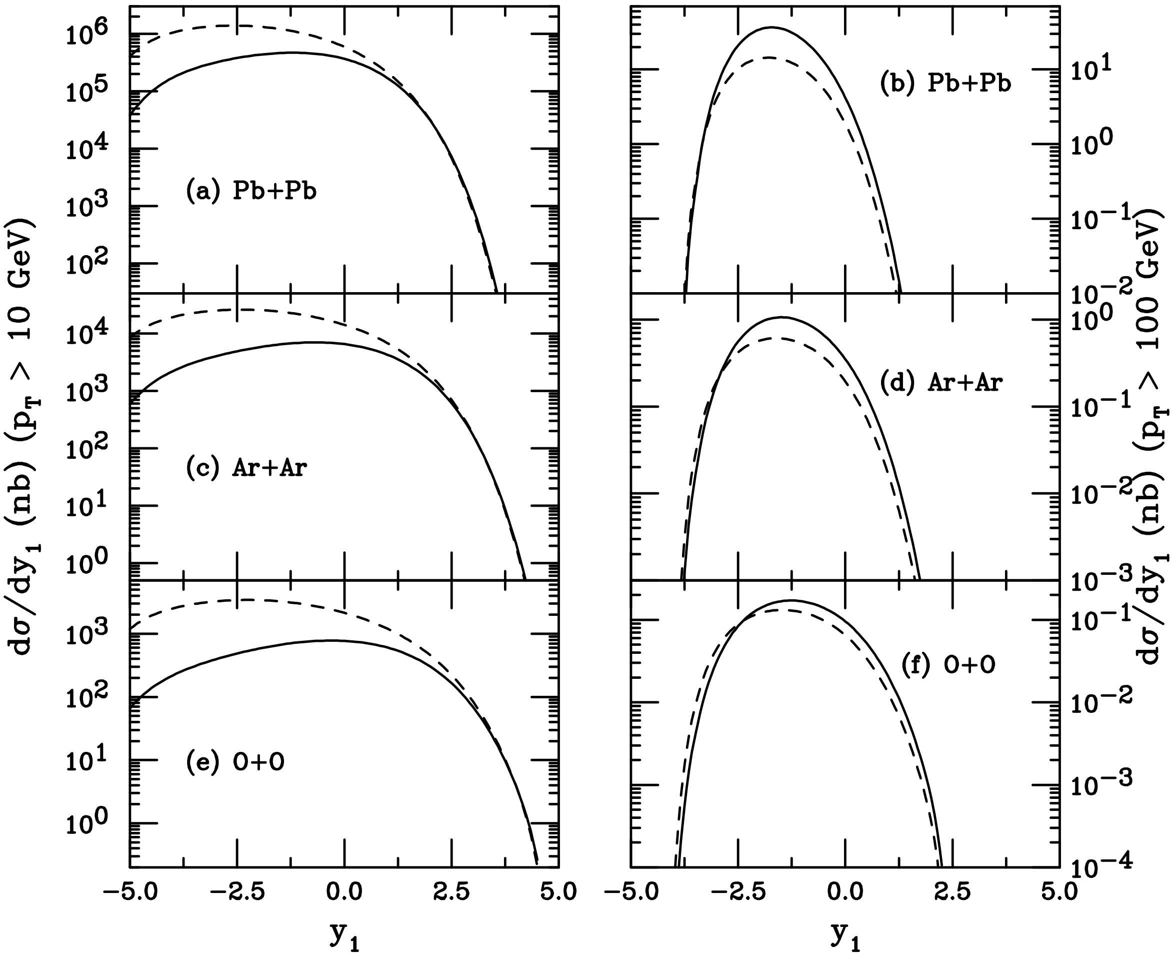

FIG. 4. We compare the rapidity distributions of direct and resolved dijet production without shadowing in peripheral collisions. The left-hand side shows the results for $p_T > 10$ GeV for (a) Pb+Pb, (c) Ar+Ar and (e) O+O collisions while the right-hand side is for $p_T > 100$ GeV for (b) Pb+Pb, (d) Ar+Ar and (f) O+O collisions. The solid curves are the direct results while the dashed curves show the resolved results. The photon is coming from the left.

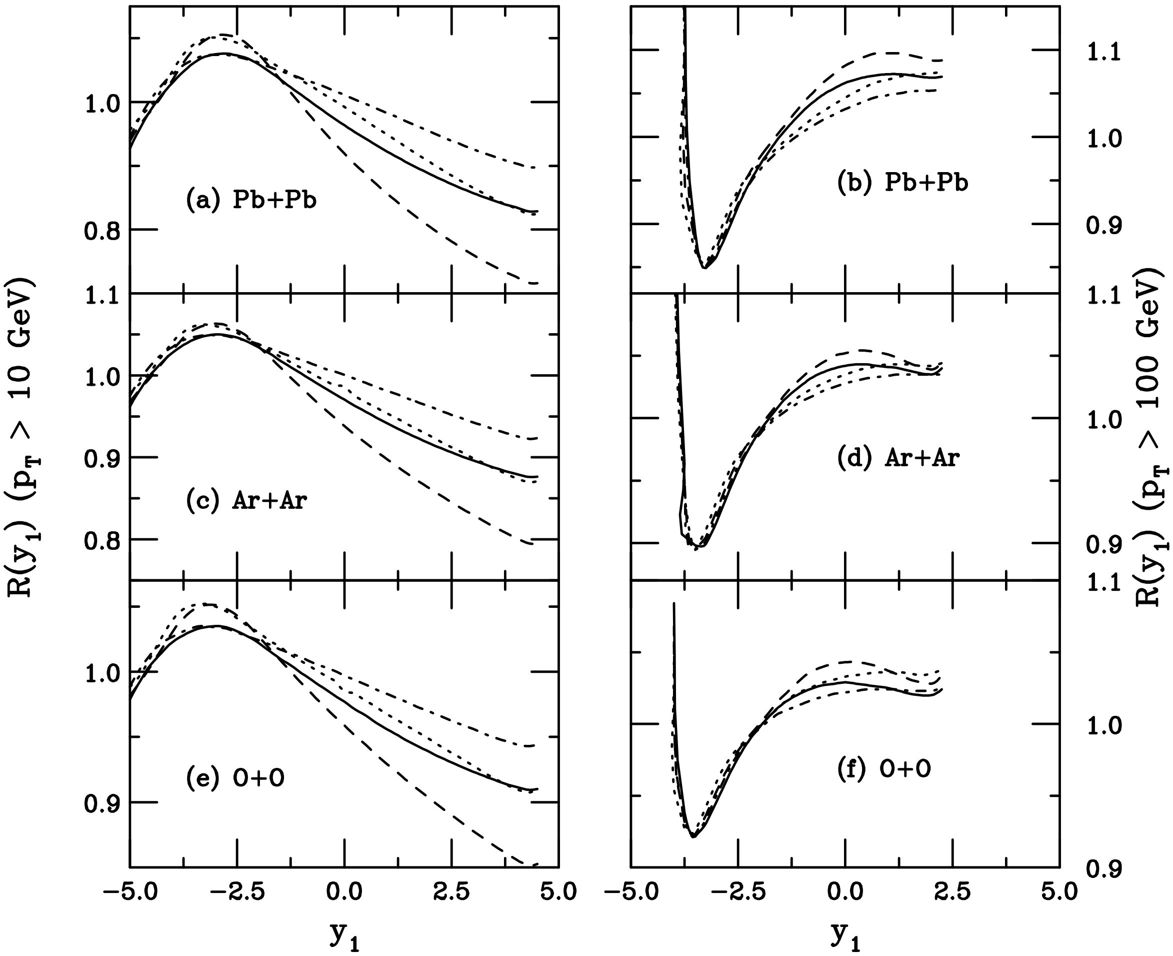

FIG. 5. We compare shadowing ratios in direct and resolved dijet production in peripheral collisions. The left-hand side shows the results for $p_T > 10$ GeV for (a) Pb+Pb, (c) Ar+Ar and (e) O+O collisions while the right-hand side is for $p_T > 100$ GeV for (b) Pb+Pb, (d) Ar+Ar and (f) O+O collisions. The solid and dashed curves give the direct ratios for the EKS98 and FGS parameterizations respectively. The dot-dashed and dotted curves show the resolved ratios for the EKS98 and FGS parameterizations respectively. The photon comes from the left. Note the difference in the y-axis scales here.

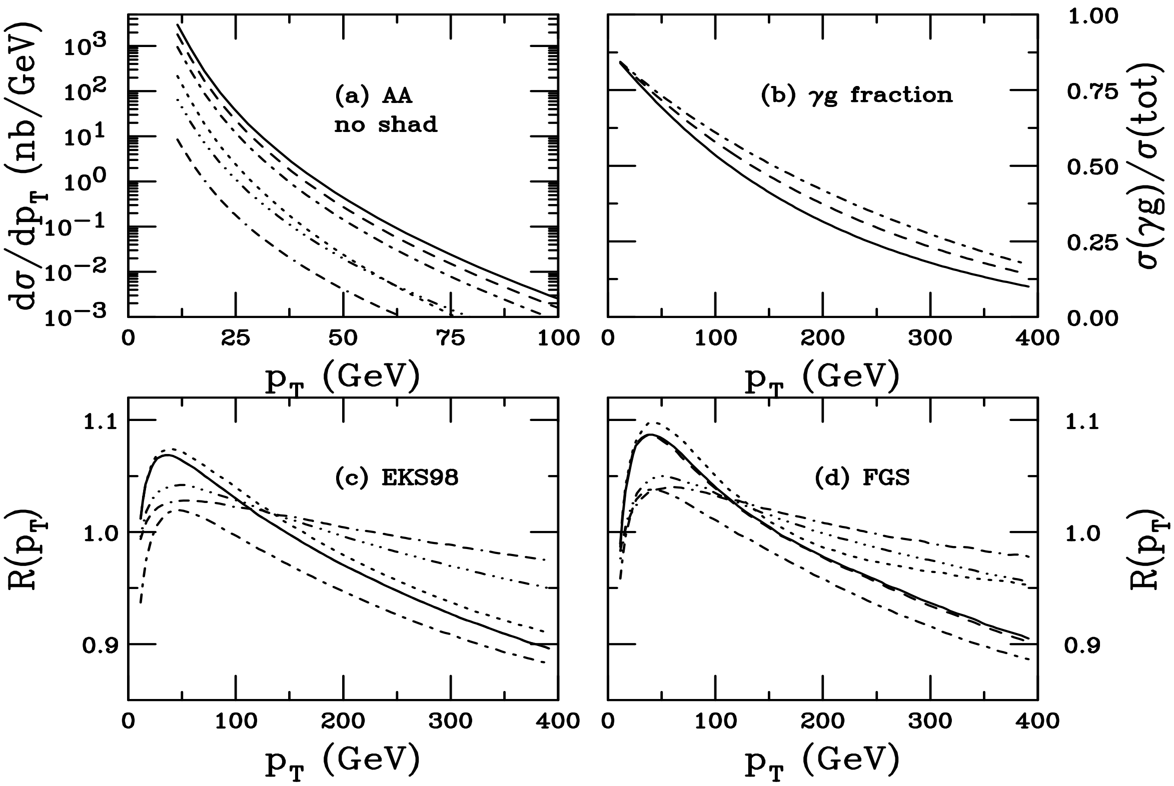

FIG. 6. Direct photoproduction of leading hadrons in peripheral collisions. (a) The p_T distributions for $|y_1| \leq 1$ are shown for AA collisions. The solid curve is the total for Pb+Pb while the produced pions (dashed), kaons (dot-dashed) and protons (dotted) are shown separately. The total production for Ar+Ar (dot-dot-dot-dashed) and O+O (dot-dash-dash-dashed) are also shown. (b) The fraction of gluon-initiated hadrons as a function of p_T. The curves are the same as in (a). (c) The EKS98 shadowing ratios for produced pions. The solid curve is the total for Pb+Pb while the ratios for pions produced by quarks (dashed), antiquarks (dotted) and gluons (dot-dashed) are shown separately. The total ratios for Ar+Ar (dot-dot-dot-dashed) and O+O (dot-dash-dash-dashed) are also shown. (d) The same as (c) for FGS.

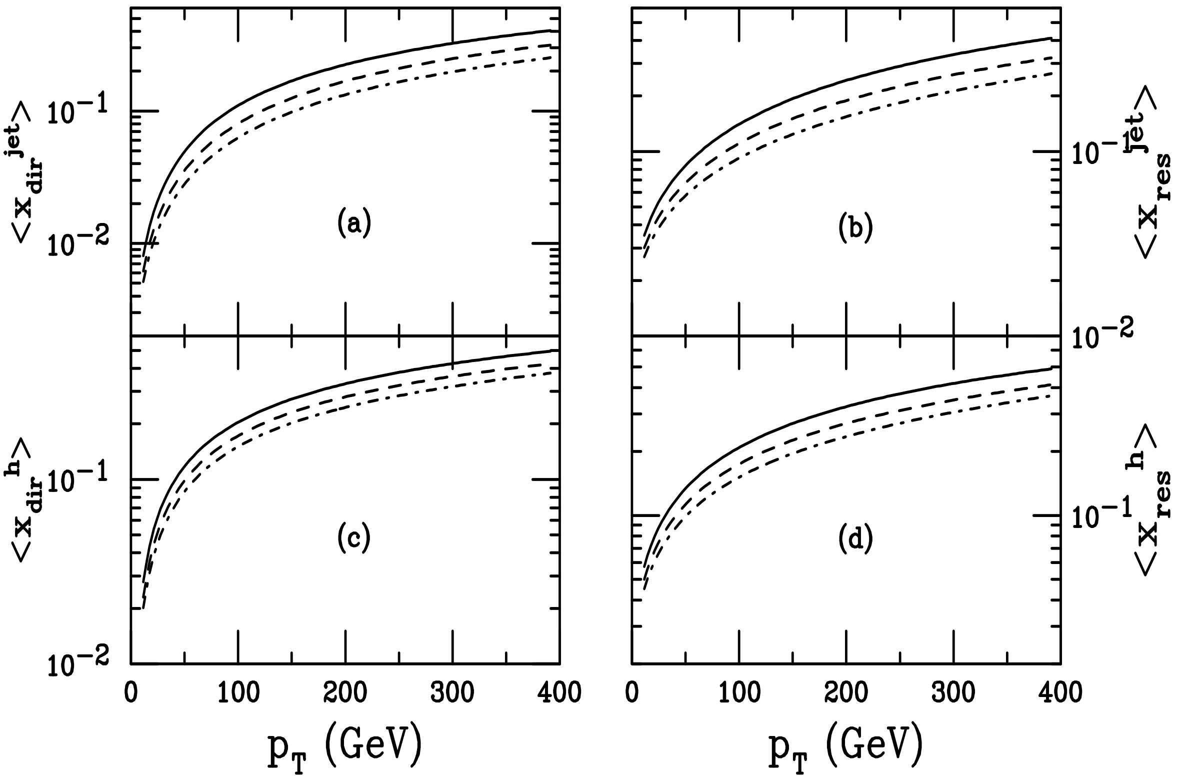

FIG. 7. The average value of the nucleon parton momentum fraction x as a function of transverse momentum. Results are given for (a) direct and (b) resolved gluon jet production and for (c) direct and (d) resolved pion production by gluons. The results are given for O+O (dot-dashed), Ar+Ar (dashed) and Pb+Pb (solid) interactions.

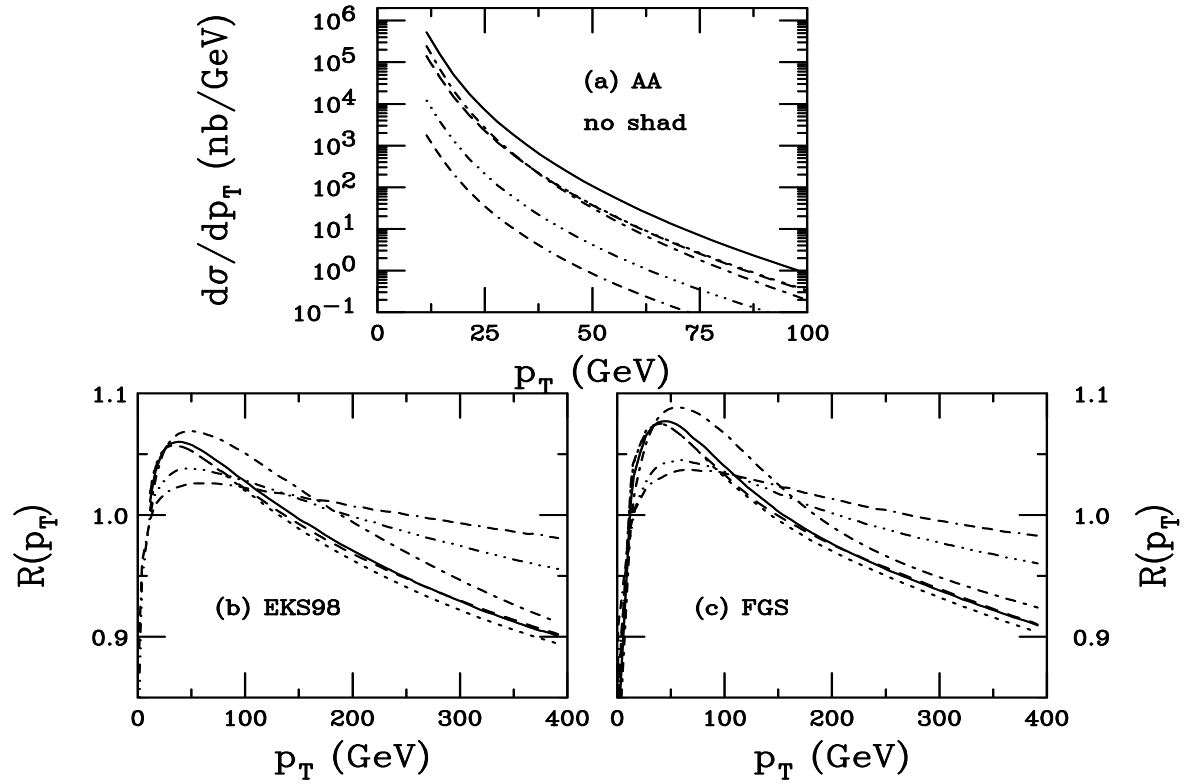

FIG. 8. Resolved dijet photoproduction in peripheral AA collisions. (a) The Pb+Pb jet p_T distributions with $|y_1| \leq 1$ are shown for quarks (dashed), antiquarks (dotted), gluons (dot-dashed) and the total (solid). We also show the total jet p_T distributions in Ar+Ar (dot-dot-dot-dashed) and O+O (dash-dash-dash-dotted) collisions. (b) The relative EKS98 shadowing contributions from quarks (dashed), antiquarks (dotted) and gluons (dot-dashed) as well as the total (solid) are shown for Pb+Pb collisions. The totals are also shown for Ar+Ar (dot-dot-dot-dashed) and O+O (dash-dash-dash-dotted) interactions. (c) The same as (b) for FGS.

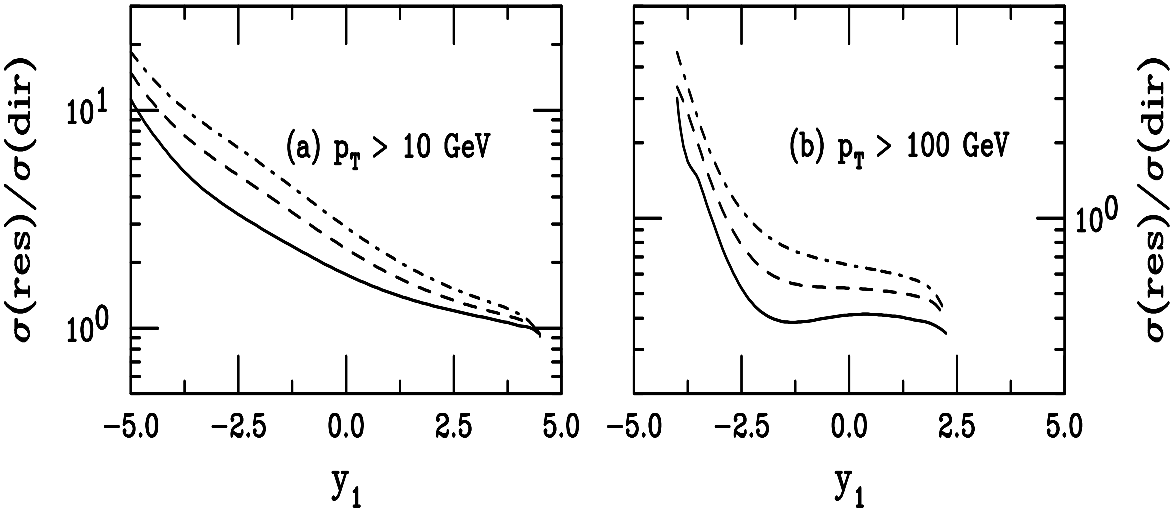

FIG. 9. We present the resolved/direct dijet production ratios as a function of rapidity. In (a) we show the results for $p_T > 10$ GeV while in (b) we show $p_T > 100$ GeV. The curves are Pb+Pb (solid), Ar+Ar (dashed) and O+O (dot-dashed). The photon comes from the left.

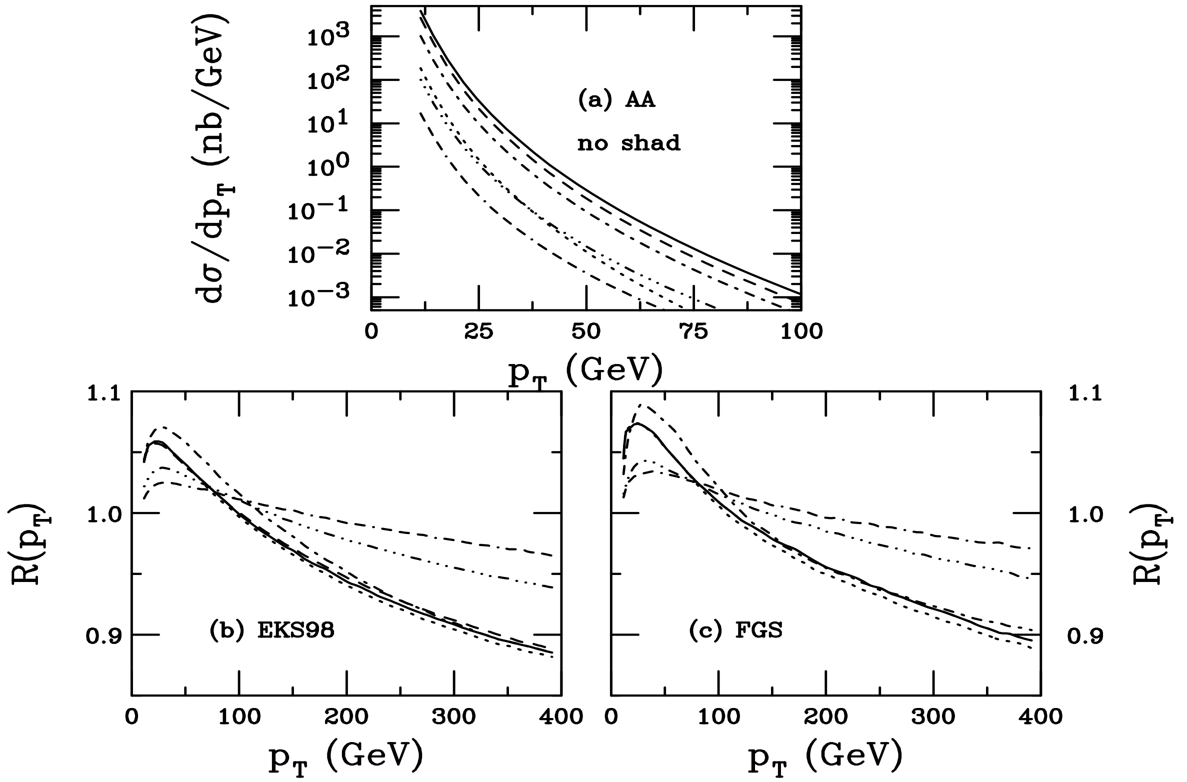

FIG. 10. Resolved leading hadrons from dijet photoproduction in peripheral collisions. (a) The p_T distributions for $|y_1| \leq 1$ are shown for AA collisions. The Pb+Pb results are shown for charged pions (dashed), kaons (dot-dashed), protons (dotted) and the sum of all charged hadrons (solid). The charged hadron p_T distributions are also shown for Ar+Ar (dot-dot-dot-dashed) and O+O (dot-dash-dash-dashed) collisions. (b) The EKS98 shadowing ratios for produced pions. For Pb+Pb collisions, we show the ratios for pions produced by quarks (dashed), antiquarks (dotted), gluons (dot-dashed) and the total (solid) separately. The ratios for pions produced by all partons are also shown for Ar+Ar (dot-dot-dot-dashed) and O+O (dot-dash-dash-dashed) collisions. (c) The same as (b) for FGS.

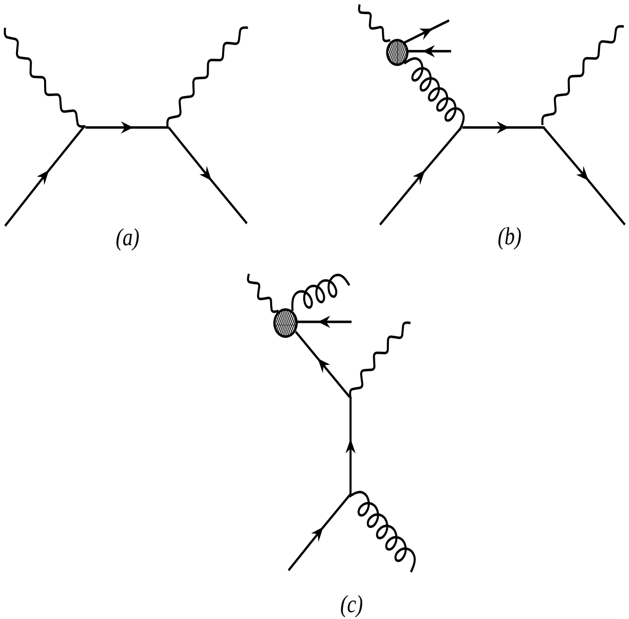

FIG. 11. Feynman diagrams for γ+jet photoproduction from direct, (a), and resolved photons, (b) and (c). Crossed diagrams are not shown.

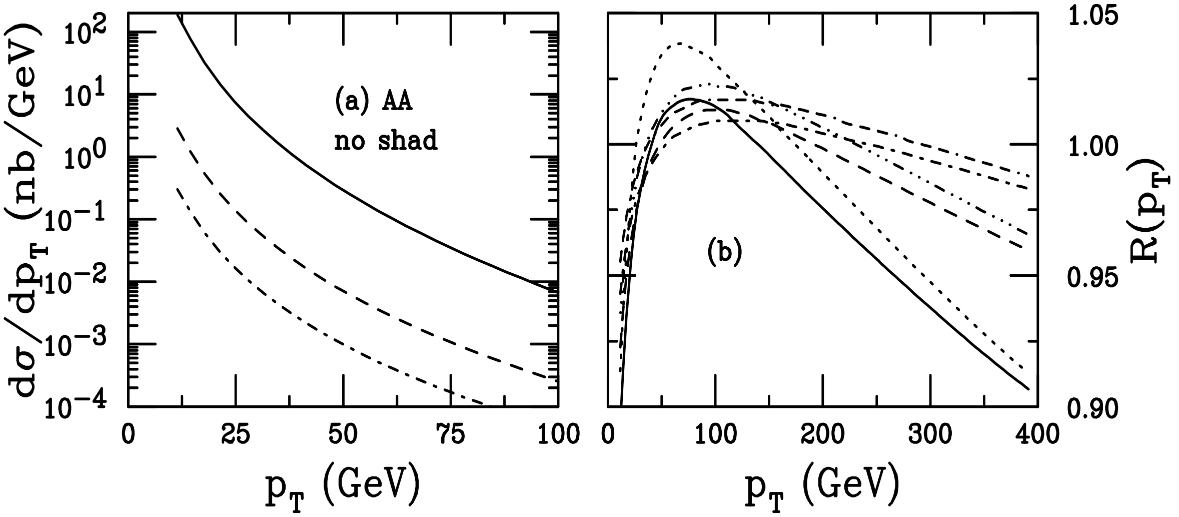

FIG. 12. Direct γ+jet photoproduction in peripheral collisions. (a) The p_T distributions for $|y_1| \leq 1$ are shown for Pb+Pb (solid), Ar+Ar (dashed) and O+O (dot-dashed) collisions. (b) The EKS98 shadowing ratios are shown for Pb+Pb (solid), Ar+Ar (dashed) and O+O (dot-dashed) while the corresponding FGS ratios are shown for Pb+Pb (dotted), Ar+Ar (dot-dot-dot-dashed) and O+O (dot-dash-dash-dashed) collisions. The photon comes from the left.

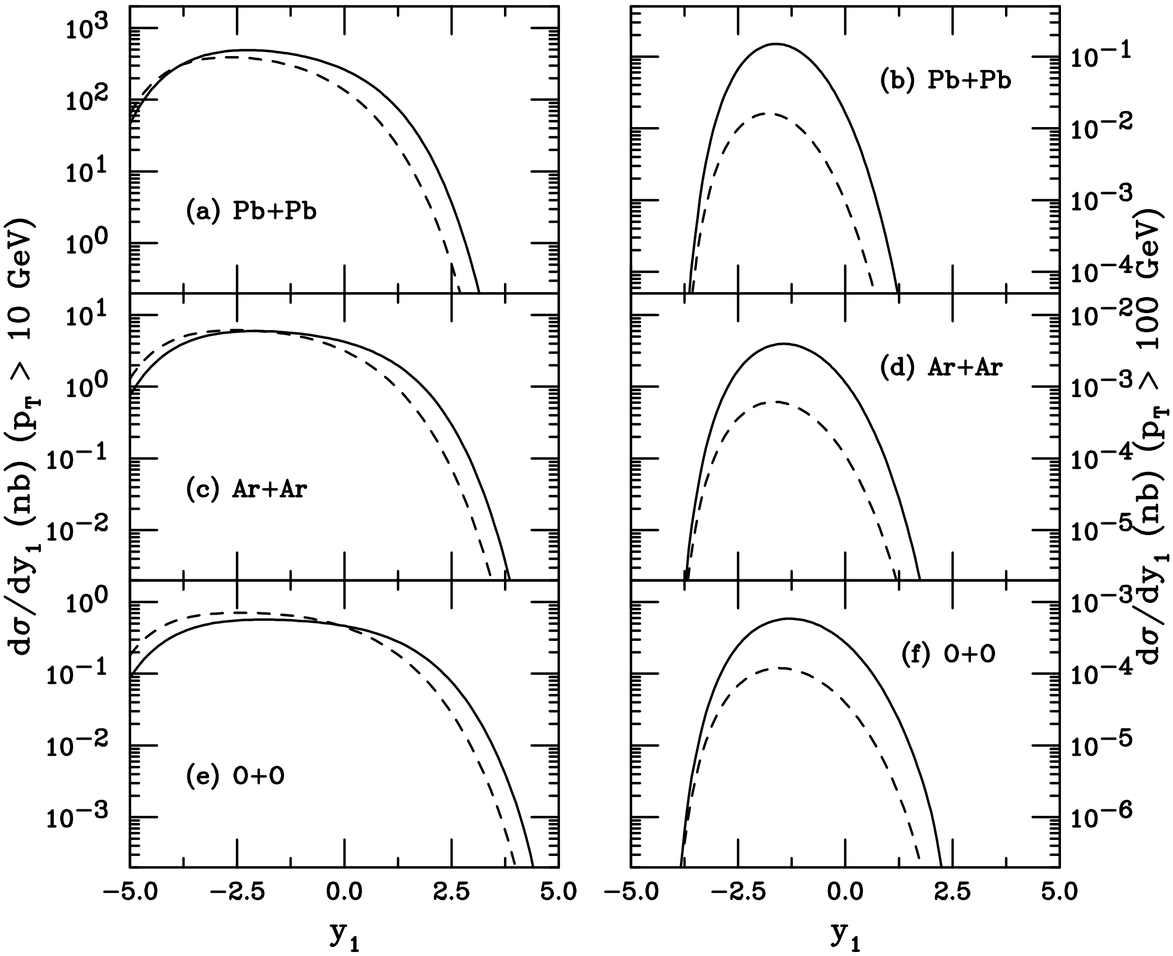

FIG. 13. We compare the rapidity distributions of direct and resolved γ+jet photoproduction in peripheral collisions. The left-hand side shows the results for $p_T > 10$ GeV for (a) Pb+Pb, (c) Ar+Ar and (e) O+O collisions while the right-hand side is for $p_T > 100$ GeV for (b) Pb+Pb, (d) Ar+Ar and (f) O+O collisions. The solid curves are the direct results while the dashed curves show the resolved results. The photon comes from the left. Note the different scales on the y-axes.

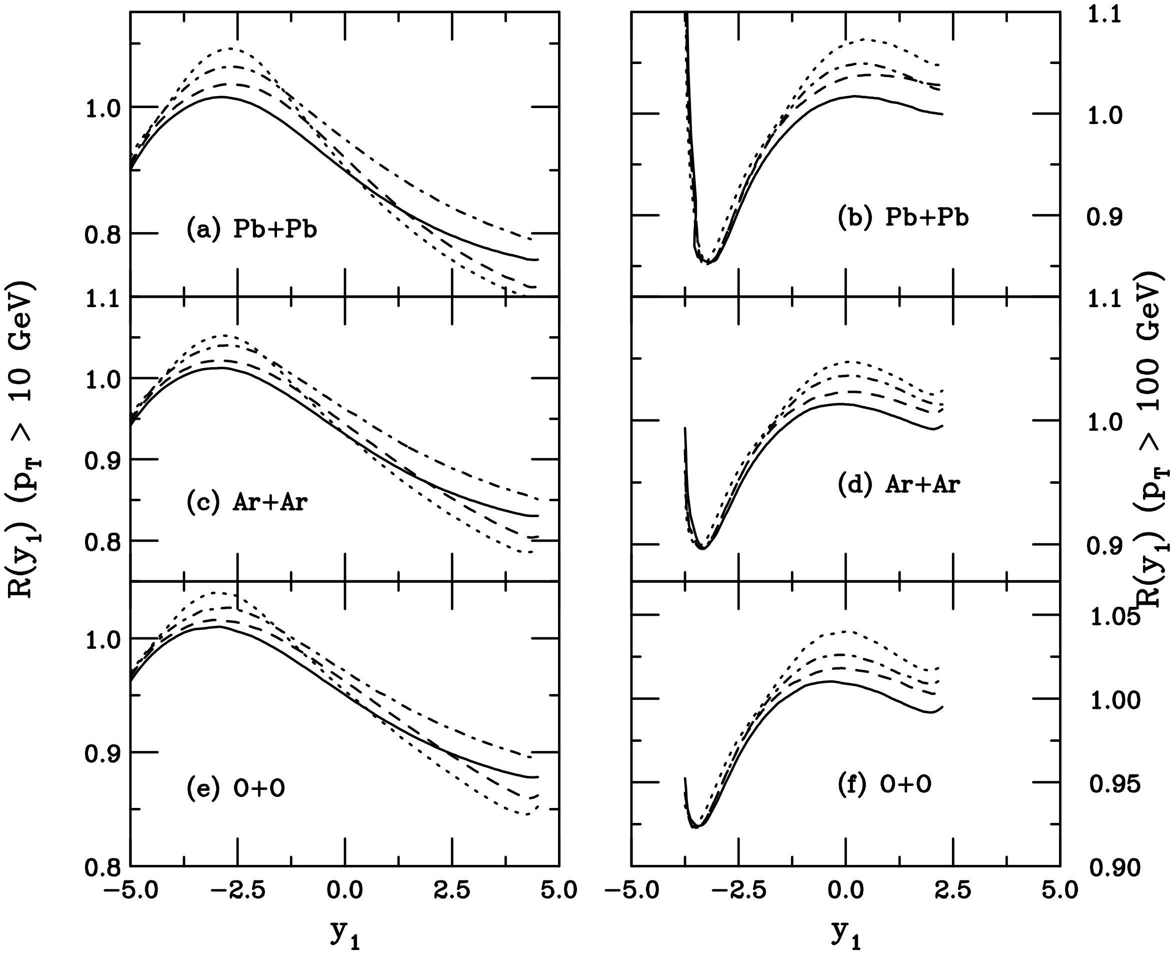

FIG. 14. We compare shadowing ratios in direct and resolved γ+jet production in peripheral collisions. The left-hand side shows the results for $p_T > 10$ GeV for (a) Pb+Pb, (c) Ar+Ar and (e) O+O collisions while the right-hand side is for $p_T > 100$ GeV for (b) Pb+Pb, (d) Ar+Ar and (f) O+O collisions. The solid and dashed curves give the direct ratios for the EKS98 and FGS parameterizations respectively. The dot-dashed and dotted curves show the resolved ratios for the EKS98 and FGS parameterizations respectively.

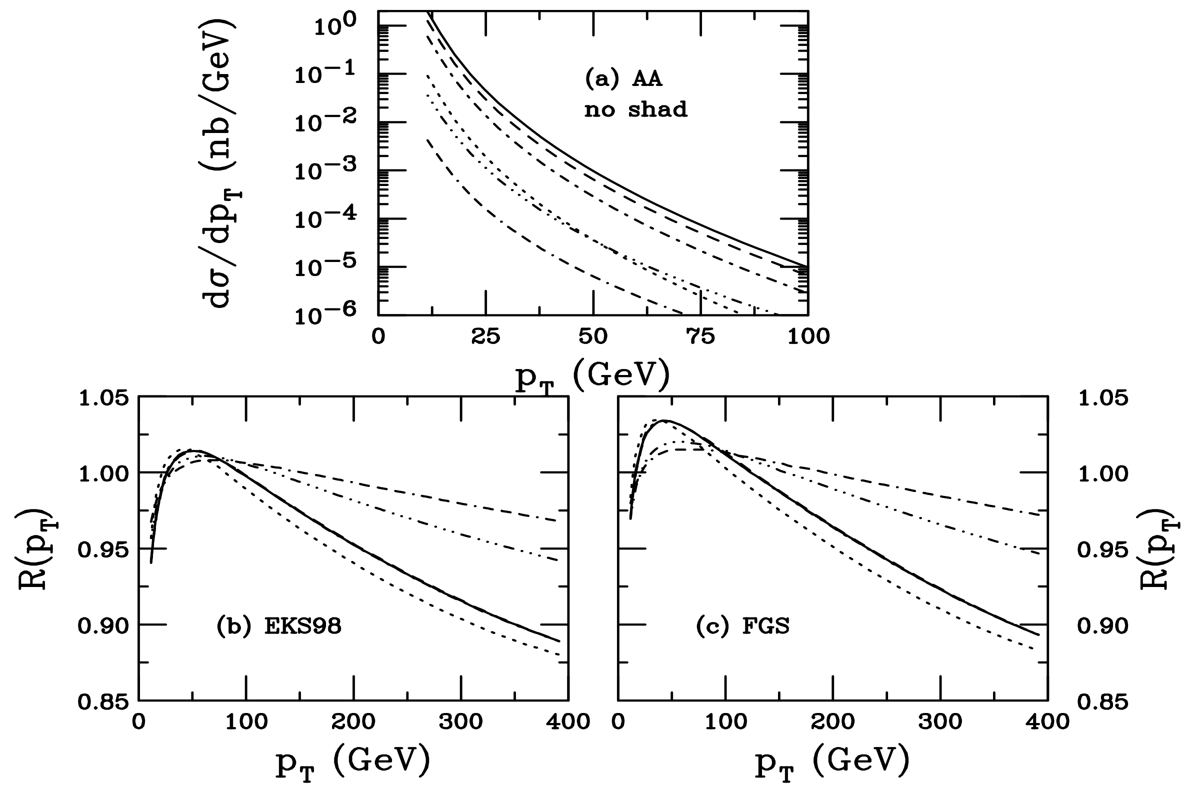

FIG. 15. Direct leading hadrons from γ+jet photoproduction in peripheral collisions. (a) The p_T distributions for $|y_1| \leq 1$ are shown for AA collisions. The Pb+Pb results are shown for charged pions (dashed), kaons (dot-dashed), protons (dotted) and the sum of all charged hadrons (solid). The charged hadron p_T distributions are also shown for Ar+Ar (dot-dot-dot-dashed) and O+O (dot-dash-dash-dashed) collisions. (b) The EKS98 shadowing ratios for produced hadrons. The results for pions, kaons and the charged hadron total (solid) are nearly identical. The proton result (dotted) is lower. The total charged hadron ratios for Ar+Ar (dot-dot-dot-dashed) and O+O (dot-dash-dash-dashed) collisions are also shown. (c) The same as (b) for FGS.

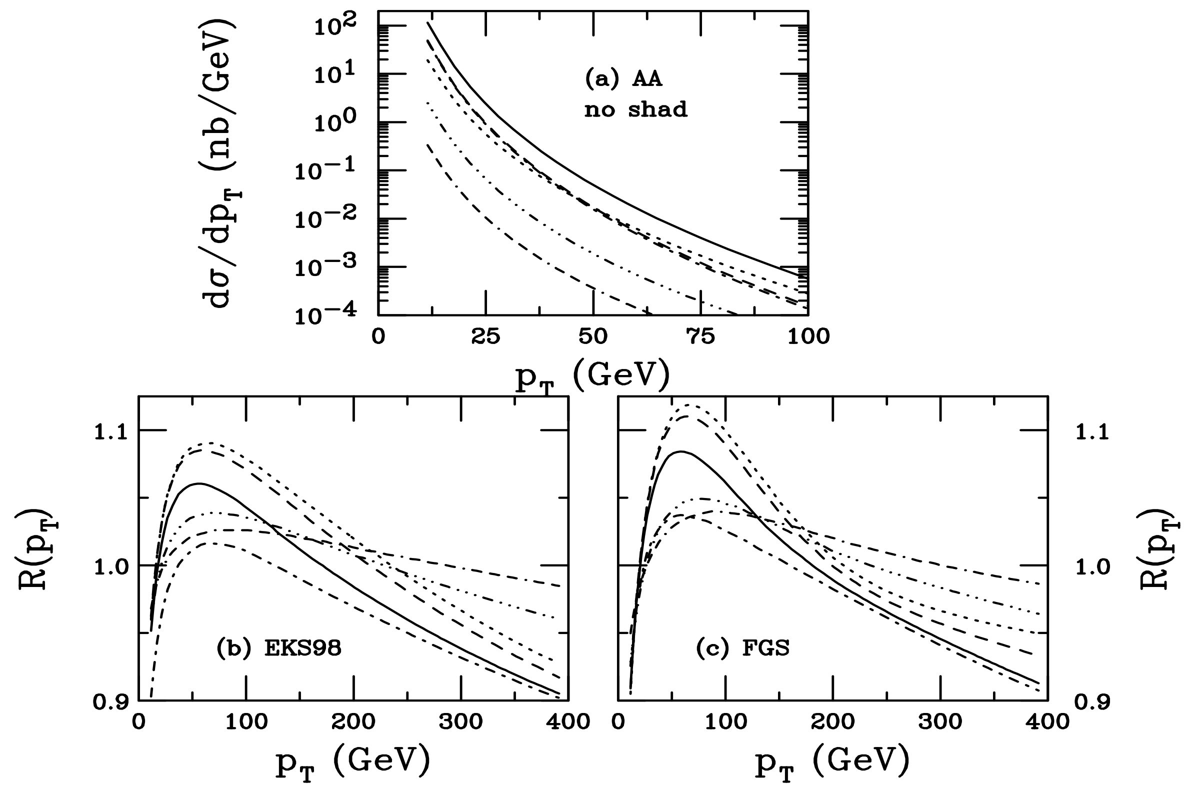

FIG. 16. Resolved γ+jet photoproduction in peripheral AA collisions. (a) The Pb+Pb jet p_T distributions with $|y_1| \leq 1$ are shown for quarks (dashed), antiquarks (dot-dashed), gluons (dotted) and the total (solid). We also show the total jet p_T distributions in Ar+Ar (dot-dot-dot-dashed) and O+O (dash-dash-dash-dotted) collisions. (b) The relative EKS98 shadowing contributions from quarks (dashed), antiquarks (dotted) and gluons (dot-dashed) as well as the total (solid) are shown for Pb+Pb collisions. The totals are also shown for Ar+Ar (dot-dot-dot-dashed) and O+O (dash-dash-dash-dotted) interactions.

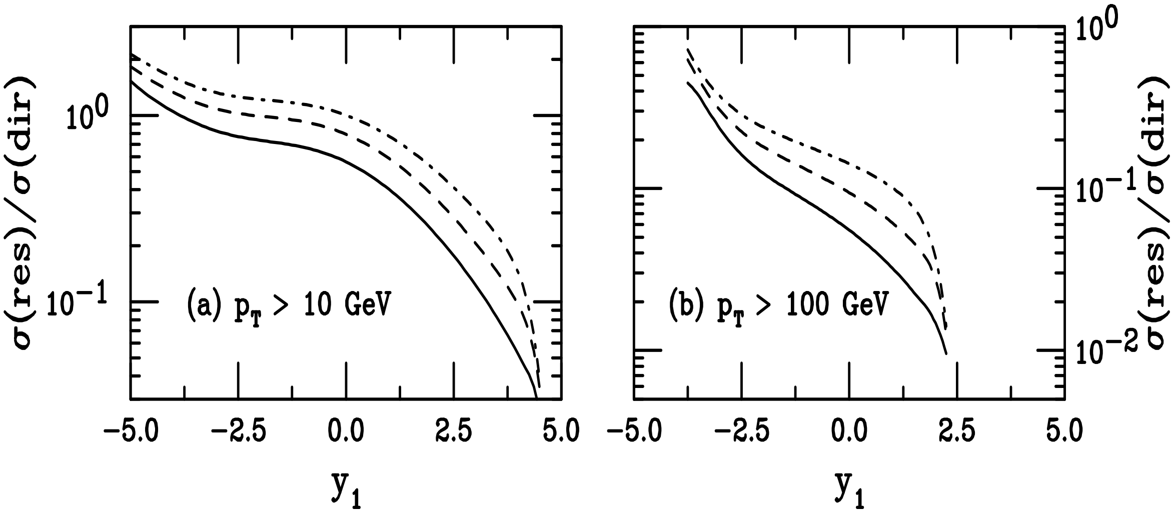

FIG. 17. We present the resolved/direct γ+jet production ratios as a function of rapidity. The left-hand side shows the results for $p_T > 10$ GeV while the right-hand side is for $p_T > 100$ GeV. The curves are Pb+Pb (solid), Ar+Ar (dashed) and O+O (dot-dashed). The photon comes from the left.

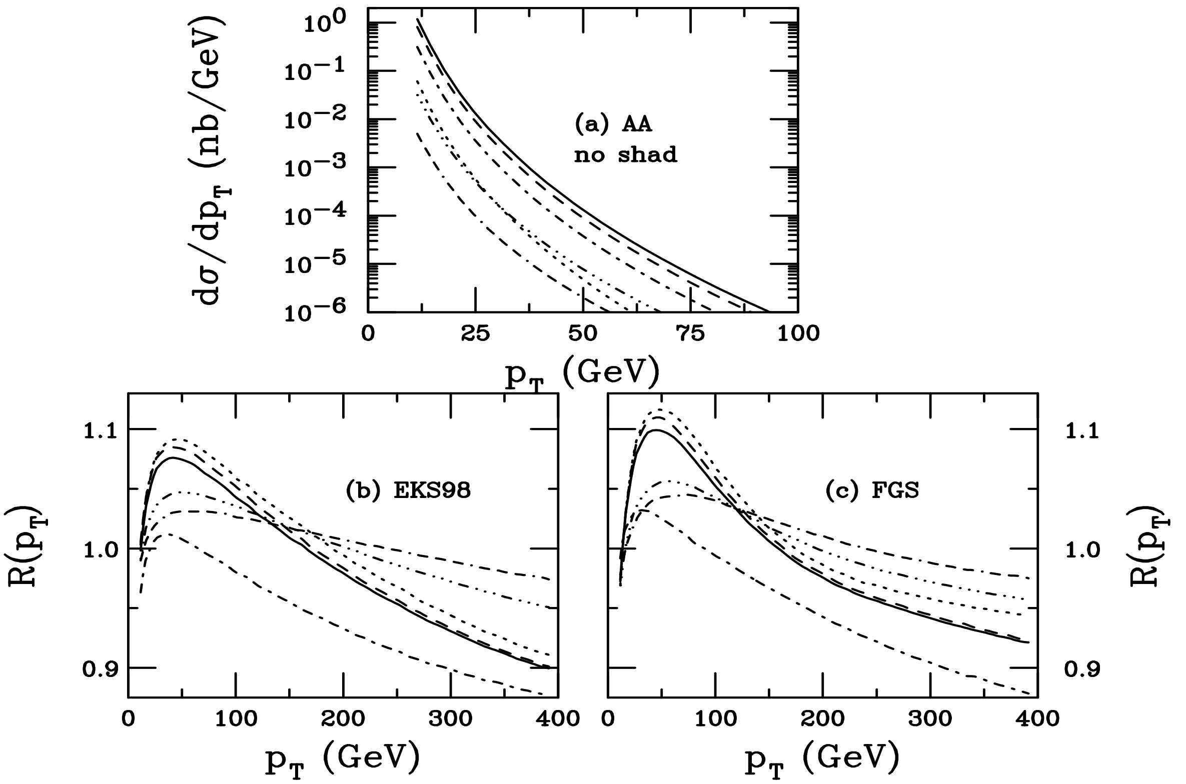

FIG. 18. Resolved leading hadrons from γ+jet photoproduction in peripheral collisions. (a) The p_T distributions for $|y_1| \leq 1$ are shown for AA collisions. The Pb+Pb results are shown for charged pions (dashed), kaons (dot-dashed), protons (dotted) and the sum of all charged hadrons (solid). The charged hadron p_T distributions are also shown for Ar+Ar (dot-dot-dot-dashed) and O+O (dot-dash-dash-dashed) collisions. (b) The EKS98 shadowing ratios for produced pions. For Pb+Pb collisions, we show the ratios for pions produced by quarks (dashed), antiquarks (dotted), gluons (dot-dashed) and the total (solid) separately. The ratios for pions produced by all partons are also shown for Ar+Ar (dot-dot-dot-dashed) and O+O (dot-dash-dash-dashed) collisions. (c) The same as (b) for FGS.